



Available online at www.sciencedirect.com

ScienceDirect

Comput. Methods Appl. Mech. Engrg. 372 (2020) 113348

Computer methods in applied mechanics and engineering

www.elsevier.com/locate/cma

A conservative level set method on unstructured meshes for modeling multiphase thermo-fluid flow in additive manufacturing processes

Stephen Lin^a, Zhengtao Gan^a, Jinhui Yan^b, Gregory J. Wagner^a,*

^a Department of Mechanical Engineering , Northwestern University, Evanston, IL, USA
^b Department of Civil and Environmental Engineering, University of Illinois at Urbana-Champaign, Urbana, IL, USA

Received 24 September 2019; received in revised form 28 July 2020; accepted 31 July 2020 Available online 25 August 2020

Abstract

Additive manufacturing (AM) is an emerging technology that fuses deposited powder materials together layer-by-layer using a localized heat source to create an arbitrarily complex geometry. This technology is an inherently multiphysics problem, involving the simultaneous evolution of fluid flow, heat transfer, free surface, laser-material interaction and material phases including solid, liquid and gas. Multiphysics and multiphase models are typically used to understand the dominant physics driving AM processes through high fidelity simulations resolving the individual powders as they melt onto the substrate. However, these types of high fidelity models have not been applicable to modeling directed energy deposition (DED) process, where powders are delivered through the ambient vapor onto the substrate by a nozzle and subsequently fused. This paper presents a novel multiphase thermo-fluid formulation for modeling DED processes. A diffuse level set formulation coupled with the Navier–Stokes, energy conservation and radiative transport equation allows us to model complex free surface, fluid flow, thermal and laser interaction evolution. In addition, our formulation enables us to resolve the vapor flow field and its effect on deposited material during AM processes. The accuracy of our proposed method is assessed by comparing with literature solutions and experimental benchmarks. Our proposed formulation is then used to model simple DED processes that enable us to visualize the entrainment of powder particles into the melt pool. This process elucidates the dominant physical forces that can drive powders into the melt pool as well as their effect on the melt pool evolution within DED processes.

Keywords: Level set method; Control volume finite element method; Additive manufacturing; Multiphase flows; Unstructured grid

1. Introduction

Additive manufacturing (AM) technologies such as directed energy deposition (DED) or powder bed fusion (PBF) have recently proven to be promising, offering many advantages including fabrication of complex geometries, manipulation of chemical compositions and microstructural control for desired mechanical properties. Many of these advantages stem from the additive process of melting thin slices together layer-by-layer to create an arbitrary 3D geometry. However, as-built products may contain defects formed during fabrication, resulting in unsatisfactory quality. This has hindered the wide industrialization of AM technologies.

E-mail address: gregory.wagner@northwestern.edu (G.J. Wagner).

^{*} Corresponding author.

The formation of defects during AM is linked to the inherently complex multiphysics and multiphase phenomena occurring during the process. A focused thermal energy source, such as a laser, melts and in some cases partially evaporates deposited material. Free surface forces, which include the recoil pressure generated from evaporation in conjunction with thermo-capillary forces, drive the flow of the molten material and cause a complex free surface evolution. These types of forces can lead to phenomena such as balling, pore formation, denudation and particle entrainment into the melt pool; all of these can have a profound impact on the as-built mechanical properties and surface finishes.

Simulations can elucidate the driving physics of this process and their dependence on processing parameters. Prior work has investigated interacting physics between free surface evolution, fluid flow and heat transfer through numerical multiphase thermal fluid models. Khairallah et al. [1,2] performed high fidelity multiphase simulations of PBF processes using the massively parallel multiphysics ALE3D code from Lawrence Livermore National Laboratories. Using this tool, they showed the dominant effects of Marangoni convection and recoil pressure in shaping the melt pool and subsequent effects such as pore formation, spattering and denudation. Körner et al. [3–5] utilized a lattice Boltzmann method (LBM) to model the PBF process in 2D. Through these simulations, they studied single layer [3] and multi-layer [4] builds; from these simulations they demonstrated the effects of powder packing on the melt characteristics such as balling. A 2D recoil pressure model was added to their model [6] to obtain better melt pool predictions. Yan et al. [7,8] utilized a volume of fluid (VoF) method to resolve the multiphase evolution of PBF processes in 3D. Through this model, phenomena such as balling and track irregularity were connected to processing parameters such as the input laser power, powder layer thickness and powder size distribution. In addition to using a VoF method to model the multiphase evolution, a discrete element method (DEM) was added [8] to model the powder spreading process for multiple layers; from this they identified inter-layer and inter-track void formation. Panwisawas et al. [9] have found similar explanations for these phenomena from their thermal fluid flow model which also utilized a VoF method within the open-source software OpenFOAM [10]. Gürtler et al. [11] also used this software and formulation to model the powder bed process to understand melting, wetting and subsequent solidification. A similar model using CFD-ACE+, a code developed by the ESI group, has been use to investigate defects such as porosity [12], balling and denudation [13]. Medina et al. [14] developed a multiphase fluid flow model to simulate DED processes. This model coupled a powder stream model to a multiphase free surface flow model within the CFD-ACE+ code. Although evaporation was not considered, this model accounted for in-flight heating and consolidation of particles into the melt pool. This model was applied to study the formation of individual and multiple tracks. More recently, Hojjatzadeh et al. [15] utilized a multiphysics-multiphase model to elucidate the effects of pore formation and elimination observed in experiments; through their simulations they found that near the laser-interaction zone, extreme thermocapillary forces can drive gaseous pores out of the melt pool.

These aforementioned multiphase thermal fluid models have elucidated the physical mechanisms that drive defect evolution such as denudation, balling and pore formation. These models, however, are not able to capture powder motion due to the surrounding gas flow; this is mainly because the modeling methods used assume the solid powder or substrate material cannot move. As a result, complex phenomenon such as powder entrainment, which has been observed in experiments [16,17], cannot be modeled. In addition, models offering a high resolution of melting, fluid flow and evaporation of individual particles have only been applied to PBF processes; models of DED processes that offer the same high fidelity multiphase thermal flow predictions are lacking.

In this work, we propose a multiphase thermal fluid model that resolves the free surface and molten pool evolution within AM processes. We demonstrate a novel capability of our method by simulating powder particles being displaced and eventually entrained by the vapor flow. This model builds off of a previous formulation demonstrated by the authors [18] and combines a traditional level set (LS) method [19–21] with the conservative level set (CLS) method [22,23] to ensure local mass conservation when discretizing our equations with a control volume finite element method (CVFEM) [24,25]. In addition, we implement an evaporation model that accounts for fluid expansion during liquid–vapor phase changes within our diffuse interface approach; this event forms a vapor jet originating from evaporating surfaces. Lastly, we propose a modified radiation transport equation (RTE) to model the laser interaction with evolving free surface. This multiphysics model enables us to visualize particle entrainment in DED processes as seen in experiments conducted by Wolff et al. [16].

The paper is organized as follows: The mathematical formulation is described in Section 2. A CVFEM discretization is briefly described and the numerical solution procedure is outlined in Section 3. Validation cases along with applications to DED process modeling are then performed and analyzed in Section 4. Conclusions are then discussed in Section 5.

2. Mathematical formulation

2.1. The level set field

2.1.1. Level set definition and properties

In the level set method, the phase interface Γ is implicitly represented by the zero level set of smooth function $\phi(x,t)$:

$$\Gamma = \{ \mathbf{x} \mid \phi(\mathbf{x}, t) = 0 \} \tag{1}$$

Away from the interface, $\phi(x, t)$ is taken to be a signed distance function to the interface Γ , and thus has the property that $|\nabla \phi| = 1$. In our formulation, we consider the level set function to be positive and negative in the metal phase and gas phase, respectively:

$$\phi(x,t) \begin{cases} > 0 & \text{if } x \in \text{metal phase} \\ = 0 & \text{if } x \in \Gamma \\ < 0 & \text{if } x \in \text{gas phase} \end{cases}$$
 (2)

It should be noted that the metal phase can be in a liquid or solid state at any time. The level set $\phi(x,t)$ is advected through the integration of an advection equation:

$$\frac{\partial \phi}{\partial t} + \mathbf{u} \cdot \nabla \phi = 0. \tag{3}$$

The advective flow field u is obtained from the solution of the Navier–Stokes equations, which will be reviewed in Section 2.6. Geometric parameters related to the interface Γ are also calculated from the level set field ϕ :

$$\mathbf{n} = \frac{\nabla \phi}{|\nabla \phi|}, \qquad \kappa = -\nabla \cdot \left(\frac{\nabla \phi}{|\nabla \phi|}\right)$$
 (4)

where n and κ are respectively the unit normal vector and curvature of the interface Γ .

To evaluate material properties such as density and viscosity, we make use of a diffuse interface formulation; properties associated with each phase (such as density and viscosity) vary smoothly across the interface over a fixed distance. A smoothed Heaviside function H_{ε} is used to separate the metal and gas phase. This function is evaluated from the distance function ϕ :

$$H_{\varepsilon}(\phi) = \left(1 + e^{-\frac{\phi}{\varepsilon}}\right)^{-1} \tag{5}$$

The parameter ε controls the interface thickness over which the smoothed Heaviside varies between close to 1 and 0; typically, this value is set to $\varepsilon = \alpha h$, where $\alpha < 1$ and h is a characteristic mesh size. This smoothed Heaviside function plays the role of a volume fraction of the metal phase (where $H_{\varepsilon} = 1$). For the numerical simulations performed in this work, we use $\alpha = \frac{1}{2}$.

Furthermore a liquid fraction field f_L will be used to further separate the metal phase into a liquid $(f_L = 1)$ or solid $(f_L = 0)$ state. This combined with H_{ε} assigns properties within the gas, liquid or solid phase:

$$\chi(\phi, f_L) = H_{\varepsilon}(\phi)(f_L \chi_{\varsigma} + (1 - f_L)\chi_I) + (1 - H_{\varepsilon}(\phi))\chi_{\sigma}$$

$$\tag{6}$$

where χ is some generic material properties (such as viscosity, density, etc.) and the subscripts s, l and g represent the material properties of the solid, liquid and gas phases, respectively

2.1.2. Redistancing of the level set

The solution to Eq. (3) does not in general preserve the signed distance property of the level set function $(|\nabla \phi| = 1)$. To re-establish this property, a redistancing operation must be performed that preserves the position of the zero level set surface. This is accomplished by solving to steady state an equation in pseudo-time τ :

$$\frac{\partial \bar{\phi}}{\partial \tau} + S_0(\phi_0)(|\nabla \bar{\phi}| - 1) = 0 \tag{7}$$

where the initial condition for Eq. (7) is the level set field at some physical time t, i.e., $\bar{\phi}(x, \tau = 0) = \phi_0(x) = \phi(x, t)$. It is assumed that $\phi_0(x)$ does not satisfy the signed distance property.

The function $S_0(\phi_0)$ is a smoothed sign function that goes to 0 at the $\phi_0 = 0$ interface:

$$S_0(\phi_0) = 2H_{\varepsilon}(\phi_0) - 1 \tag{8}$$

Eq. (7) can be reformulated as an advection equation. Using $|\nabla \bar{\phi}| = \nabla \bar{\phi} \cdot \frac{\nabla \bar{\phi}}{|\nabla \bar{\phi}|}$ and rearranging results in

$$\frac{\partial \bar{\phi}}{\partial \tau} + \boldsymbol{w} \cdot \nabla \bar{\phi} = S_0(\phi_0) \tag{9}$$

where the redistancing velocity \boldsymbol{w} is defined as:

$$\mathbf{w} = S_0(\phi_0) \frac{\nabla \bar{\phi}}{|\nabla \bar{\phi}|} \tag{10}$$

It can be seen from the form of the redistancing equation in Eq. (9) that information is propagated away from the stationary interface to recover the signed distance property of $\bar{\phi}$. The analytical solution to the steady state (in pseudo time) version of Eq. (9) satisfies $|\nabla \bar{\phi}| = 1$ and is equal to ϕ_0 where $\phi_0 = 0$, and thus gives the signed distance to the $\phi_0 = 0$ interface; the solution to this equation is therefore used to replace the current level set field $\phi(x,t)$. A numerical discretization of Eq. (7) will introduce mass error in the individual phases, because the zero level set contour does not remain stationary during redistancing. As a result, we need a method of enforcing local mass conservation throughout the simulation.

2.2. The volume fraction field

The level set formulation presented in Section 2.1 provides a flexible way of implicitly resolving the interface and calculating geometric quantities of the interface using Eq. (4). However, there is no guarantee that the volume fraction H_{ε} is transported in a conservative manner; this is a well known problem with level set methods. To this end, we follow Olsson and Kreiss [22] and Olsson et al. [23] and introduce an additional equation to transport the volume fraction H_{ε} in a conservative manner and enforce local volume conservation over the level set field:

$$\frac{\partial H_{\varepsilon}}{\partial t} + \nabla \cdot (\boldsymbol{u} H_{\varepsilon}) = \nabla \cdot [\gamma(\varepsilon \nabla H_{\varepsilon} - H_{\varepsilon}(1 - H_{\varepsilon})\boldsymbol{n})] \tag{11}$$

where ε is the same parameter expressed in Eq. (5) and n has the same definition from Eq. (4). Eq. (11) is written in a conservative form, with a flux given by the quantity inside square brackets; as a result we can expect that the total volume fraction within the domain will be conserved throughout time. Note that the form of H_{ε} given in Eq. (5) leads to zero flux, indicating that Eq. (5) gives the steady solution to Eq. (11) when the velocity is 0.

The two terms inside the square brackets on the right hand side ensure that the volume fraction profile does not become too diffuse over time from numerical diffusion; the first term within the brackets on the right hand side diffuses the volume fraction, and is counteracted by the second term that acts as a compressive flux to maintain a sharp profile. Thus, γ acts as a resharpening speed, and is generally taken to be the local magnitude of the velocity. It should be noted that we use a method similar to the one proposed by Desjardin et al. [26]; we first advect the level set field with Eq. (3) and compute n with Eq. (4) to be used in the volume fraction transport Eq. (11). Eq. (5) is then used to obtain a mass-conserving signed distance field ϕ near the free surface from the updated field H_{ε} . Redistancing of the field ϕ is finally performed with Eq. (9) to ensure that the level set field respects the signed distance property $|\nabla \phi| = 1$.

2.3. The temperature field

To obtain the temperature field, we solve the energy conservation equation:

$$\rho c_p \frac{\partial T}{\partial t} + \rho c_p \nabla \cdot (\boldsymbol{u}T) + \rho L \frac{\partial f_L}{\partial t} + \rho L \nabla \cdot (\boldsymbol{u}f_L) = \nabla \cdot (k \nabla T) + Q_{sf}$$
(12)

where T is the temperature field, ρ is the material density, c_p is the material specific heat, k is the thermal conductivity, L is the material latent heat of fusion and f_L is the local liquid volume fraction. The third and fourth terms on the left-hand side account for changes in energy due to solidification or melting; the method of modeling this will be reviewed in Section 3.4. The term Q_{sf} in Eq. (12) is an energy source term; this term represents the

energy fluxes applied on the free surface. Since we are using a diffuse representation of the free surface Γ , we use a continuum surface force (CSF) [27] method to apply the fluxes as a volumetric source term. We account for radiative and laser fluxes in Q_{sf} , but do not account for convective fluxes; this is captured by the advective cooling due to the fluid velocity at the free surface:

$$Q_{sf} = Q_{rad} + Q_{laser} + Q_{evap} \tag{13}$$

where the radiative cooling term Q_{rad} is defined as:

$$Q_{rad} = \sigma_{SB} \epsilon \left(T^4 - T_{\infty}^4 \right) |\nabla H_{\varepsilon}| \tag{14}$$

where σ_{SB} is the Stefan-Boltzmann constant, ϵ is the material emissivity, T_{∞} is the ambient temperature. The gradient of the smoothed Heaviside plays the role of a smoothed Dirac delta function, smoothing the surface flux into a volumetric source with the correct integrated value through the thickness of the interface. Similarly, evaporative cooling term Q_{evap} is defined as:

$$Q_{evap} = L_v m_{evap} \left| \nabla H_{\varepsilon} \right| \tag{15}$$

where L_v is the latent heat of vaporization and m_{evap} is the net evaporation mass flux, which is described in Section 2.4. The term Q_{laser} is applied in a different manner, and will be discussed in Section 2.5.

2.4. Evaporation modeling

As the metal–gas interface temperature reaches the boiling or evaporation point (T_{evap}) , evaporation begins to occur. A Knudsen layer, which is several mean free path lengths thick, forms right above the evaporating surface; within this layer the evaporating gas is in a state of thermodynamic non-equilibrium. Theoretical models for the evaporation kinetics in these regimes have been developed, such as those proposed by Knight [28] and Anisimov [29]; in this manuscript we use the kinetic evaporation model developed by Anisimov [29]. This model predicts discontinuities in quantities such as the temperature or pressure across the Knudsen Layer. From this model, a net evaporation mass flux m_{evap} can be calculated:

$$m_{evap} = P_{sat}(T) \left(\frac{m_{mol}}{2\pi R_{gas} T} \right) \tag{16}$$

where R_{gas} is the gas constant, m_{mol} is the molar mass of the evaporating species and $P_{sat}(T)$ is the saturation pressure at temperature T. The saturation pressure can be calculated through the Clausius-Clapeyron relation:

$$P_{sat}(T) = P_{amb} \exp\left(\frac{-L_v m_{mol}}{R_{gas}} \left(\frac{1}{T} - \frac{1}{T_{evap}}\right)\right)$$
(17)

where T_{evap} is the evaporation temperature at a given ambient pressure P_{amb} . Lastly, a recoil pressure resulting from momentum conservation due to vapor expansion during evaporation acts on the free surface. The model used in this manuscript is the one proposed by Anisimov [29]:

$$P_{recail} = 0.54 P_{sat}(T) \tag{18}$$

For the this work, the gas constant is $R = 8.314 \frac{J}{K \text{ mol}}$ and the ambient pressure is 101 kPa.

2.5. Radiative transport equation

A radiative transport equation (RTE) models the propagation of the laser beam. The RTE has the following general form:

$$\nabla \cdot (\mathbf{s}I) + (\mu_A + \mu_S)I = \frac{\mu_A \sigma_{SB} T^4}{\pi} + \frac{\mu_s}{4\pi} G \tag{19}$$

where I is the beam intensity (with units of W/m²) traveling along direction s, μ_A is the absorption opacity, μ_S is the scattering opacity, and G is the incident radiative energy due to scattering from other surfaces. In this work, we neglect any scattering ($\mu_S = 0$) and energy absorbed by the laser due to surface emissions (first term on the

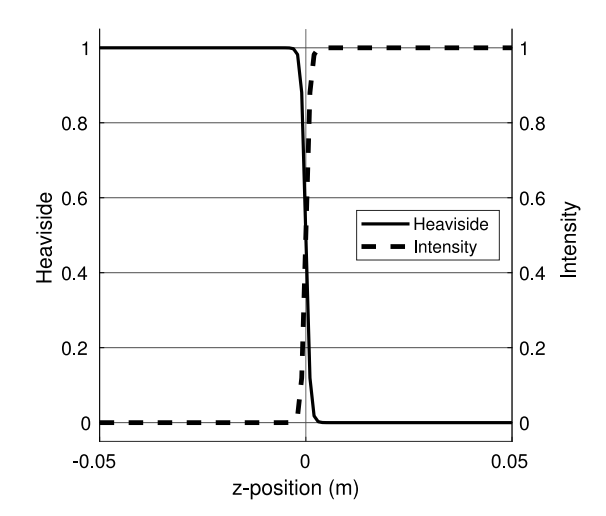


Fig. 1. 1D example of spatial profile of intensity I and Heaviside H_{ε} .

right hand side of Eq. (19). We will also assume that s will always be in the negative z-direction. This results in the reduced form of the RTE:

$$\nabla \cdot (\mathbf{s}I) + \mu_A I = 0 \tag{20}$$

The absorption opacity is dependent on the free surface location. Furthermore, we assume that the laser is fully absorbed through the thickness of the diffuse interface; this means the laser is fully absorbed at the free surface, and does not spread into the volume of the material. This is similar to using a ray-tracing method [30] without accounting for subsequent reflections of the beam upon absorption. We derive a form of μ_A that achieves this by considering a 1D example, as shown in Fig. 1. In this example, the laser intensity enters from the left domain, and the free surface is situated at the center. An ideal solution that enforces the intensity to be absorbed through the thickness of the interface is $I_{ideal} = 1 - H_{\varepsilon}$. Substituting this solution into Eq. (20) with $s = -\mathbf{e}_z$ results in:

$$-\frac{dI_{ideal}}{dz} + \mu_A I_{ideal} = -\frac{d}{dz} (1 - H_{\varepsilon}) + \mu_A (1 - H_{\varepsilon}) = 0$$
(21)

Solving Eq. (21) for μ_A yields:

$$\mu_A = -\frac{\partial H_{\varepsilon}}{\partial z} \left(\frac{1}{1 - H_{\varepsilon} + \varepsilon_{small}} \right) \tag{22}$$

where ε_{small} is a small number to avoid division by 0.

At the top vertical surface Γ_{top} , a Dirichlet boundary condition is applied that describes the profile of the laser. For the following cases, we have assumed a Gaussian profile of the laser:

$$I = \frac{2\eta P}{\pi r_h^2} \exp\left(-\frac{2r^2}{r_h^2}\right) \quad \text{on } \Gamma_{top}$$
 (23)

where r is the radial distance from an integration point to the laser focal point, P is the input power, η is a laser absorption coefficient between 0 and 1 and r_b is the beam radius. With the beam intensity field I, we can define the laser source term Q_{laser} in Eq. (13):

$$Q_{laser} = \left| \frac{\partial I}{\partial z} \right| \tag{24}$$

Here, we have assumed that the laser acts in the z-direction.

2.6. Incompressible two-phase flow

Incompressible two-phase flow is governed by the Navier-Stokes equation:

$$\rho(\phi, f_L) \left(\frac{\partial \boldsymbol{u}}{\partial t} + \nabla \cdot (\boldsymbol{u}\boldsymbol{u}) \right) = -\nabla p + \nabla \cdot \left(\mu(\phi, f_L)(\nabla \boldsymbol{u} + \nabla \boldsymbol{u}^T) \right) + \rho(\phi, f_L) \boldsymbol{g} \beta (T - T_{ref}) + \boldsymbol{f}_{sf} + A \boldsymbol{u}$$
(25)

$$\nabla \cdot \boldsymbol{u} = m_{evap} \boldsymbol{n} \cdot \nabla (\frac{1}{\rho}) \tag{26}$$

where u is the flow velocity, p is the hydrostatic pressure, β is the coefficient of thermal expansion (CTE) and g is the gravitational acceleration. A Boussinesq approximation [31] is used to model buoyancy forces. The material density $\rho(\phi, f_L)$ and viscosity $\mu(\phi, f_L)$ are calculated according to Eq. (6). The additional source term in the continuity equation in Eq. (26) accounts for fluid expansion due to local evaporation at the free surface; this model is similar to those proposed by Courtois et al. [32–34] and Esmaeeli and Tryggvason [35]. A derivation of the form of Eq. (26) is presented in the Appendix. As a result, incompressibility is satisfied within the metal and gas phases individually, but does not hold at the free surface. The last term in Eq. (25) is a source term that inhibits the velocity flow development in the solid phase ($f_L = 0$) and goes to zero in the liquid phase ($f_L = 1$). The form of A is taken from the Kozeny–Carman permeability of a packed bed:

$$A = C \frac{(1 - f_L)^2}{f_L^3 + b} \tag{27}$$

where C is a very large number and b is a small number to avoid division by 0; this term is commonly used to model solidification, and is described by Voller et al. [36] and Rösler and Brüggemann [37]. The term f_{sf} is a continuum surface force (CSF) [27] discretization of any interfacial forces that act over the interface Γ . The following interfacial forces are considered:

$$f_{sf} = f_{Marangoni} + f_{evaporation} + f_{recoil} + f_{ST}$$
(28)

where $f_{Marangoni}$ is the Marangoni force, $f_{evaporation}$ is the force due to the fluid expansion during evaporation, f_{recoil} is the recoil pressure and f_{ST} is a surface tension force. Due to conservation of momentum, a pressure jump shifted towards the gas phase will be implicitly induced due to the fluid expansion term in Eq. (26). The evaporation force in the momentum equation (28) balances the jump in momentum as fluid crosses the interface. This force is given by the gradient of the momentum normal to the interface, m_{evap}^2/ρ :

$$f_{evaporation} = \nabla \left(\frac{m_{evap}^2}{\rho} \right) \tag{29}$$

An additional recoil pressure force is applied at the free surface; this force incorporates the momentum imparted upon the free surface from vaporizing material, and is responsible for the formation of keyholes:

$$f_{recoil} = P_{recoil} \nabla H_{\varepsilon} \tag{30}$$

where P_{recoil} is defined in Eq. (18). The surface tension force f_{ST} is given as:

$$f_{ST} = \sigma(T)\kappa(\phi)\nabla H_{\varepsilon} \tag{31}$$

where $\sigma(T)$ is the surface tension coefficient and κ is defined in Eq. (4). The surface tension coefficient $\sigma(T)$ is dependent on the temperature T, and is assumed to have a linear relationship:

$$\sigma(T) = \sigma_0 + \frac{\partial \sigma}{\partial T}(T - T_0) \tag{32}$$

where T_0 and σ_0 are the reference temperature and surface tension coefficient, respectively. Large thermal gradients at the free surface will lead to gradients in the surface tension coefficient; this will induce a convective Marangoni force defined as:

$$f_{Marangoni} = \frac{\partial \sigma}{\partial T} \left(\nabla T - \mathbf{n} (\mathbf{n} \cdot \nabla T) \right) |\nabla H_{\varepsilon}| \left(\frac{2\rho}{\rho_L + \rho_G} \right)$$
(33)

where $\partial \sigma/\partial T$ is the temperature coefficient of surface tension and the last term on the right in parenthesis is used to shift this force towards the dense (liquid) phase.

2.7. Turbulence model

At high enough energy densities, the heated material may begin to vaporize. This vaporization will create a recoil pressure, pushing out molten material to create a large cavity in the workpiece called a keyhole; keyhole modes induce fluctuating velocity fields and enhance the rates of momentum, heat and mass transport within the molten pool. A turbulence model is considered to calculate the effective viscosity and thermal conductivity to account for this enhanced transport. These effective values vary spatially and are dependent on the characteristics of the flow field. Here, we adopt a vorticity-based mixing length turbulence model that is similar to the one used by Rai et al. [38] to model weld pools exhibiting keyholing phenomena in stainless steel and aluminum; predicted weld pool shapes with this turbulence model resulted in good agreement with experimental data. For a distance y_{wall} away from the melt pool wall boundary, the mixing length l_{mix} is given by:

$$l_{mix} = \kappa_{mix} y_{mall} \tag{34}$$

Here, the melt pool wall boundary is defined as the solidus isotherm during the computation and $\kappa_{mix} = 0.41$. The turbulent viscosity μ_T is then computed as:

$$\mu_T = \rho l_{mix}^2 |\omega| \tag{35}$$

where $|\omega|$ is the magnitude of the flow vorticity $(\nabla \times \boldsymbol{u})$. The turbulent thermal conductivity k_T is obtained from the definition of the turbulent Prandtl number Pr_T :

$$k_T = \frac{\mu_T c_p}{\Pr_T} \tag{36}$$

For the current calculations, $Pr_T = 0.9$ [39].

3. Numerical formulation

In this work, a control volume finite element method (CVFEM) formulation is used to spatially discretize the governing equations reviewed in Section 2. This method combines the local, discrete conservation properties associated with finite volumes with the geometric flexibility of finite element interpolation functions. The governing equations are posed in a conservative integral form and applied to discrete control volumes. Surface and volumetric integrations are then evaluated using finite element interpolation techniques. CVFEM utilizes discrete control volumes constructed around each node within a finite element mesh; Fig. 2 shows this for a patch of 2D quadrilateral elements. Volumes are formed by connecting the centers of elements, edges, and (in 3D) faces of the original finite element mesh, forming a polygonal or polyhedral control volume (CV). An individual element includes a sub-portion of the CVs associated with each of its connected nodes; these sub-portions are referred to as sub-control volumes (SCV), and the faces bounding them as sub-control surfaces (SCS). The following sections briefly discusses the CVFEM discretization of the mathematical model formulated in Section 2. A more in-depth description of CVFEM is available in the literature [18,42,43].

3.1. Incompressible two-phase flow

The two-phase Navier–Stokes equation posed in Eqs. (25) and (26) is first posed in an integral form for each control volume Ω_I with a bounding surface Γ_I . Invoking the divergence theorem and assuming density is constant over Ω_I results in:

$$\rho_{I} \left(\int_{\Omega_{I}} \frac{\partial \boldsymbol{u}}{\partial t} d\Omega_{I} + \int_{\Gamma_{I}} (\boldsymbol{u}\boldsymbol{u}) \cdot \bar{\boldsymbol{n}} d\Gamma_{I} \right) = \int_{\Omega_{I}} (\rho_{I}\boldsymbol{g} + \boldsymbol{f}_{sf} + A\boldsymbol{u}) d\Omega_{I} + \int_{\Gamma_{I}} (\mu(\nabla \boldsymbol{u} + \nabla \boldsymbol{u}^{T}) - p\boldsymbol{I}) \cdot \bar{\boldsymbol{n}} d\Gamma_{I}$$
(37)

$$\int_{\Gamma_I} \boldsymbol{u} d\Gamma_I = m_{evap,I} \boldsymbol{n} \cdot \int_{\Gamma_I} \frac{1}{\rho} \bar{\boldsymbol{n}} d\Gamma_I \tag{38}$$

¹ Hughes et al. [40] and Hughes and Wells [41] have demonstrated that the finite element method is globally and locally conservative under the right conditions. However, as will be shown, the CVFEM solution of the Navier–Stokes equation gives a velocity field that satisfies mass conservation discretely at each control volume, ensuring local conservation of advected scalar fields such as volume fraction.

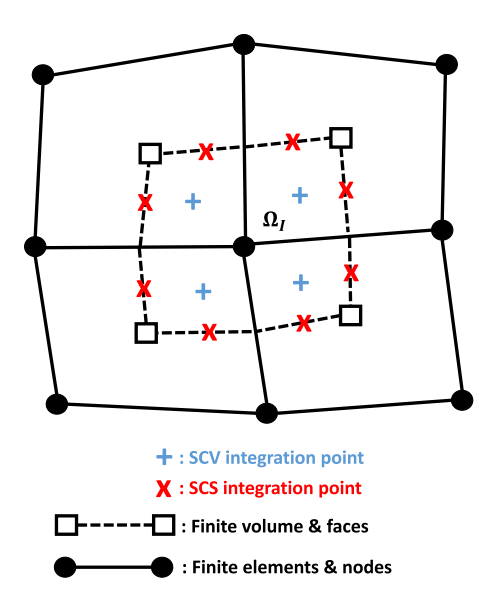


Fig. 2. A 2D control volume centered about a finite element node in a collection of 2D quadrilateral elements.

where \bar{n} is the outward pointing normal from surface Γ_I and I is the identity tensor. In Eq. (38), we also assume that the interface unit normal n and mass evaporation flux m_{evap} are constant over a control volume Ω_I . A CVFEM discretization is then carried out by approximating surface integrals at the SCS integration points and volumetric integrals at the nodes (which are at the center of each Ω_I). We use a backward Euler time integration scheme with a collocated projection method [44,45] to update velocity and pressure variables. Using the variable density fractional step formulation proposed by Almgren et al. [46], we first solve for an intermediate velocity \hat{u} with an initial pressure guess p^* .

$$\rho_{I}^{n+1} \left(\frac{\hat{\boldsymbol{u}}_{I} - \boldsymbol{u}_{I}^{n}}{\Delta t} \Delta V_{I} + \sum_{ip=1}^{n_{scs}} \hat{\boldsymbol{u}}_{adv,ip} \dot{\boldsymbol{v}}_{ip}^{n} \right) = \rho_{I}^{n+1} \boldsymbol{g} \Delta V_{I} + \boldsymbol{f}_{sf,I} \Delta V_{I} + A \hat{\boldsymbol{u}} \Delta V_{I}$$

$$+ \sum_{ip=1}^{n_{scs}} \left(\mu_{ip} (\nabla \hat{\boldsymbol{u}}_{ip} + \nabla \hat{\boldsymbol{u}}_{ip}^{T}) + p_{ip}^{*} \boldsymbol{I} \right) \cdot \bar{\boldsymbol{n}}_{ip} \Delta A_{ip}$$

$$(39)$$

where n_{scs} is the number of SCS integration points and n_{scv} is the number of SCV integration points. Furthermore, ΔA_{ip} is the surface area at a SCS integration point and ΔV_I is the nodal volume of Ω_I ; the location of these computed quantities with respect to the control volume are shown in Fig. 2. The volume flow rate \dot{v}_{ip} , the expression for which is given below, approximates $\mathbf{u}_{ip} \cdot \mathbf{n} \Delta A_{ip}$ over the SCS and is a function of the integration point velocities, pressures and interfacial forces. The advected velocity $\mathbf{u}_{adv,ip}$ in (39) is an upwinded value that is evaluated based on the sign of \dot{v}_{ip} (see [18] for details). After solving for a new pressure field p^{n+1} to enforce continuity (see below), the updated velocity at time t^{n+1} can then be computed:

$$\mathbf{u}_{I}^{n+1} = \hat{\mathbf{u}}_{I} - \frac{\Delta t}{\rho_{I}^{n+1}} (\nabla p_{I}^{n+1} - \nabla p_{I}^{*})$$
(40)

In this expression, the pressure gradient at the nodes is evaluated according to a lumped L_2 projection based on the divergence theorem:

$$\nabla p_I = \frac{1}{\Delta V_I} \sum_{ip=1}^{n_{scs}} p_{ip} \bar{\boldsymbol{n}}_{ip} \Delta A_{ip} \tag{41}$$

Eq. (41) can be modified to evaluate nodal gradients for any scalar value. We extend our previous formulation for an unstructured balanced force algorithm [18] to account for both the surface tension and recoil pressure

forces:

$$\boldsymbol{f}_{ST,I} = \frac{\sigma \kappa_I}{\Delta V_I} \sum_{ip=1}^{n_{scs}} H_{ip} \bar{\boldsymbol{n}}_{ip} \Delta A_{ip}, \quad \boldsymbol{f}_{recoil,I} = \frac{P_{recoil,I}}{\Delta V_I} \sum_{ip=1}^{n_{scs}} H_{ip} \bar{\boldsymbol{n}}_{ip} \Delta A_{ip}$$
(42)

The nodal curvature κ , which is a second derivative in the level set field ϕ is computed as:

$$\kappa_I = \frac{1}{\Delta V_I} \sum_{ip=1}^{n_{scs}} \frac{\nabla \phi_{ip}}{|\nabla \phi_{ip}|} \cdot \bar{\boldsymbol{n}}_{ip} \Delta A_{ip} \tag{43}$$

where $\nabla \phi_{ip}$ is divided by its norm $|\nabla \phi_{ip}|$ to compute the interface unit normal vector \mathbf{n} at Γ . The volume flow rate \dot{v}_{ip} at the integration point takes a form similar to Eq. (40), but with the pressure gradients evaluated at the integration point to avoid decoupling between the pressure and velocity fields on collocated meshes [47,48]. To discretely balance the pressure gradient, both the surface tension and recoil pressure force are also evaluated at the integration point:

$$\dot{v}_{ip}^{n+1} = \left(\hat{\boldsymbol{u}}_{ip} + \Delta t \left[\left(\frac{\nabla p^*}{\rho^{n+1}} \right)_{ip} - \left(\frac{\boldsymbol{f}_{ST}}{\rho^{n+1}} \right)_{ip} - \left(\frac{\boldsymbol{f}_{recoil}}{\rho^{n+1}} \right)_{ip} \right. \\
\left. - \left(\frac{1}{\rho^{n+1}} \right)_{ip} \left(\nabla p_{ip}^{n+1} - \sigma_{ip} \kappa_{ip} \nabla H_{ip} - P_{recoil,ip} \nabla H_{ip} \right) \right] \right) \cdot \bar{\boldsymbol{n}}_{ip} \Delta A_{ip} \tag{44}$$

where the form of interpolation for integration point values marked as $(\cdot)_{ip}$ are described by Lin et al. [18]. Other integration point values marked with subscript ip are evaluated as:

$$\Phi_{ip} = \sum_{I=1}^{n_N} N_I^{ip} \Phi_I, \qquad \nabla \Phi_{ip} = \frac{\partial \Phi_{ip}}{\partial x_j} = \sum_{I=1}^{n_N} \frac{\partial N_I^{ip}}{\partial x_j} \Phi_I \tag{45}$$

where Φ is some general variable, n_N is the number of nodes within an element and N_I^{ip} is the finite element shape function at a node I evaluated at an SCS or SCV integration point. The pressure at the new time step is determined by enforcing that the volume flow rates satisfy the continuity equation (38), leading to a Poisson equation for p^{n+1} :

$$\sum_{ip=1}^{n_{scs}} \Delta t \left(\frac{1}{\rho^{n+1}}\right)_{ip} \nabla p_{ip}^{n+1} \cdot \bar{\boldsymbol{n}}_{ip} \Delta A_{ip} = \sum_{ip=1}^{n_{scs}} \left(\hat{\boldsymbol{u}}_{ip} + \Delta t \left[\left(\frac{\nabla p^*}{\rho^{n+1}}\right)_{ip} - \left(\frac{\boldsymbol{f}_{ST}}{\rho^{n+1}}\right)_{ip} + -\left(\frac{\boldsymbol{f}_{recoil}}{\rho^{n+1}}\right)_{ip} + \left(\frac{1}{\rho^{n+1}}\right)_{ip} \left(\sigma_{ip} \kappa_{ip} \nabla H_{ip} + P_{recoil,ip} \nabla H_{ip}\right)\right]\right) \cdot \bar{\boldsymbol{n}}_{ip} \Delta A_{ip}$$

$$m_{evap,I} \boldsymbol{n}_{I} \cdot \sum_{ip=1}^{n_{scs}} \left(\frac{1}{\rho}\right)_{ip} \bar{\boldsymbol{n}}_{ip} \Delta A_{ip}$$

$$(46)$$

3.2. Discretization of general scalar transport equations

The transport equation for a general scalar quantity Φ is:

$$\frac{\partial \Phi}{\partial t} + \nabla \cdot (\boldsymbol{u}\,\Phi) - \nabla \cdot (D\nabla\Phi) = S \tag{47}$$

in this current work, Φ can represent the level set (ϕ) , volume fraction (H_{ε}) , intensity (I) or temperature (T) field. The parameter D is a general diffusivity coefficient and S on the right hand side represents any source/sink terms; this includes any CSF terms applying boundary conditions at the free surface. Invoking the divergence theorem allows Eq. (47) to be put into conservative integral form:

$$\int_{\Omega_I} \frac{\partial \Phi}{\partial t} d\Omega_I + \int_{\Gamma_I} \Phi \mathbf{u} \cdot \mathbf{n} d\Gamma_I - \int_{\Gamma_I} D\nabla \Phi \cdot \mathbf{n} d\Gamma_I = \int_{\Omega_I} S d\Omega_I$$
 (48)

A CVFEM spatial and backward Euler time discretization of Eq. (48) results in

$$\left(\frac{\Phi_I^{n+1} - \Phi_I^n}{\Delta t}\right) \Delta V_I + \sum_{ip=1}^{n_{scs}} \left(\Phi_{upw,ip}^{n+1} \dot{\boldsymbol{v}}_{ip}^n - D_{ip} \nabla \Phi_{ip} \cdot \boldsymbol{n}_{ip} \Delta A_{ip}\right) = S_I \Delta V_I \tag{49}$$

where $\Phi_{upw,ip}$ is an upwinded value based on \dot{v}_{ip} . The discretized transport equation (49) will be used to discretize the level set (Eq. (3)), volume fraction (Eq. (11)), radiative transport (Eq. (20)) and temperature equation (Eq. (12)).

Discretization of advective transport requires additional stabilization. For our formulation, this stabilization is implemented by incorporating upwinding for evaluating integration points located at sub-control faces corresponding to a local control volume. A detailed description of this advection stabilization process is given by Lin et al. [18] and Domino [42].

3.3. Level set redistancing

Analytically, Eq. (7) preserves the position of the zero level set of $\phi(x,t)$ in pseudo-time. However, as mentioned in Section 2.1.2, a numerical solution of this equation introduces discretization errors that will inevitably perturb the zero level set surface. These errors are small at each pseudo-time step, but accumulation can cause a substantial change in mass over time. This mass loss over time can be substantially reduced by using the volume fraction H_{ε} to enforce local mass conservation over each cell. To do this, we recover a new level set field near the interface by inverting the updated volume fraction field using Eq. (5); this level set field will be used as an initial condition for subsequent redistancing by Eq. (7).

We approximate the reinitialization velocity w as constant over the control volume, allowing us to formulate the advection term as a surface integral using the divergence theorem:

$$\int_{\Omega_I} \frac{\partial \bar{\phi}}{\partial \tau} d\Omega_I = -\mathbf{w}_I \cdot \int_{\Gamma_I} (\bar{\phi} \mathbf{n}) d\Gamma_I + \int_{\Omega_I} S_0(\phi_0) d\Omega_I$$
(50)

A CVFEM discretization of Eq. (50) results in:

$$\left(\frac{\bar{\phi}_I^{k+1} - \bar{\phi}_I^k}{\Delta \tau}\right) \Delta V_I = -\boldsymbol{w}_I \cdot \left(\sum_{ip=1}^{n_{scs}} \bar{\phi}_{upw,ip}^{k+1} \boldsymbol{n}_{ip} \Delta A_{ip}\right) + S_0(\phi_0) \Delta V_I \tag{51}$$

where the upwinded quantity $\bar{\phi}_{upw,ip}^{k+1}$ depends on local redistancing velocity w_I dotted with the area normal $n_{ip}\Delta A_{ip}$.

3.4. Source-based method for solidification

The energy equation (12) requires the simultaneous solution of two variables, T^{n+1} and f_L^{n+1} . To solve this, a method proposed by Voller et al. [49] is used to iteratively update f_L^{k+1} and T^{k+1} in a consistent manner to model solidification, where the superscript k is introduced as an iterative counter. We present a brief overview of this method in this section, but interested readers should refer to the work by Voller et al. [49] for a detailed explanation. The variable f_L^{k+1} is linearized with a Taylor series expansion:

$$f_L^{k+1} = f_L^k + \frac{dF}{dT}(T^{k+1} - F^{-1}(f_L^k))$$
(52)

where F(T) is a function that evaluates f_L from T. For the current work, we assume a piece-wise linear function for F(T):

$$f_L = F(T) = \begin{cases} 0, & T < T_S \\ \frac{T - T_S}{T_L - T_S}, & T_S \le T \le T_L \\ 1, & T_L < T \end{cases}$$
 (53)

where T_S and T_L are the solidus and the liquidus temperature, respectively. From Eq. (52) it can be seen that f_L^{k+1} is written in terms of the previously iterated f_L^k and the current temperature being iterated upon T^{k+1} . We can insert Eq. (52) into the discretization of Eq. (12) to solve for T^{k+1} . The most updated value of T^{k+1} is then used to update f_L^{k+1} using Eq. (52). Once convergence is met, the temperature and liquid fraction are updated by $T^{n+1} = T^{k+1}$ and $f_L^{n+1} = f_L^{k+1}$, respectively.

3.5. Solution algorithm

The solution algorithm for our proposed thermal multiphase model is summarized as follows:

- 1. Update any turbulence quantities as needed using the algebraic model described in Section 2.7
- 2. Solve for the velocity and pressure field using the fractional step algorithm outlined in Section 3.1
- 3. Store the conservative volume fluxes \dot{v}_{ip} at the SCS integration points
- 4. Solve the level set advection Eq. (3) and store off n to use in Eq. (11)
- 5. Solve for volume fraction transport Eq. (11)
- 6. Compute ϕ as a function H_{ε} near the free surface by inverting Eq. (5) to enforce local volume conservation.
- 7. Solve for the redistanced level set field $\bar{\phi}^{k+1}$ using ϕ^{n+1} as an initial condition
- 8. Solve for the beam intensity field I from Eq. (20)
- 9. Iteratively solve for the temperature and liquid fraction field from Eq. (12) using the methodology proposed by Voller et al. [49]
- 10. Calculate viscosity and density fields from Eq. (6) and curvatures and normal from Eq. (4)
- 11. Repeat steps 1 to 10 until a desired time state is reached

Note, the algorithm outlined above is for modeling additive manufacturing processes that involve a heat source. For the following simulations, the redistancing algorithm listed in step 7 is run until the level set field is redistanced up to 5 element lengths on either side of the interface. The advection of the level set and the Navier–Stokes solution algorithm is carried out with second-order upwinding with van Leer slope limiters enforced. This formulation has been implemented in Nalu, an open-source, massively parallel, generalized unstructured CVFEM code developed at Sandia National Laboratories for low Mach number flows [42] and built upon the Trilinos linear solver package [50]. The base Nalu code has shown good weak and strong parallel scalability for problems up to 9 billion fluid elements across 131,072 processors [51], and has further shown good scalability for a similar multiphase algorithm [18].

4. Results

4.1. Thermocapillary droplet migration

The thermocapillary migration of a droplet is used as a validation case for the thermal multiphase solver. Fig. 3 shows the initial conditions for this 2D problem. A droplet is suspended in an ambient liquid with a linear initial temperature profile in the absence of gravity. The top and bottom surfaces of the domain are fixed with temperatures of T_{high} and T_{low} , respectively; no-slip boundary conditions are applied at these surfaces as well. The temperatures at these surfaces are offset from a reference value T_0 , creating an initial temperature gradient $|\nabla T|$ of 200 k/m across the domain. All other domain boundaries are modeled with a no-penetration and adiabatic boundary condition. The droplet itself has a radius of $a = 1.44 \times 10^{-3}$ m; the domain itself is a square with a length of 5.76×10^{-3} m.

This problem can be characterized by the reference velocity W_r , Reynolds number Re, Marangoni number Ma and Capillary number Ca, which are defined as:

$$W_r = \frac{|\frac{\partial \sigma}{\partial T}||\nabla T|a}{\mu}, \quad Re = \frac{\rho a W_r}{\mu}, \quad Ma = \frac{\rho c_p a W_r}{k}, \quad Ca = \frac{\mu W_r}{\sigma}$$
 (54)

Ma and Bothe [52] have performed this same simulation, and investigated the effects of domain size on the terminal rise velocity; for this particular case a domain size is chosen such that the wall distance is two times the droplet diameter. In addition, we run this simulation for three different mesh sizes of 16, 32 and 64 elements across the droplet diameter to measure convergence. Material properties are chosen such that Re = 0.72, Ma = 0.72 and Ca = 0.0576 when parameters are computed using the droplet properties. The ratios of the material properties ρ , μ and c_p between the droplet and the ambient liquid are chosen to be 0.5. Absolute values for the ambient liquid material properties are $\rho_l = 500 \text{ kg/m}^3$, $\mu_l = 0.024 \text{ Pa s}$, $k_l = 2.4 \times 10^{-6} \text{ W/(m K)}$, $c_{p,l} = 1 \times 10^{-4} \text{ J/(kg K)}$, $\sigma = 1 \times 10^{-2} \text{ N/m}$ and $\frac{\partial \sigma}{\partial T} = -2 \times 10^{-3} \text{ N/(m K)}$.

Fig. 4 shows the velocity direction and temperature field once the droplet has reached a terminal rise velocity. The surface tension is higher in regions of lower temperature, resulting in a surface tension gradient or Marangoni effect. This Marangoni effect induces a flow direction around the bubble surface from lower to higher temperatures.

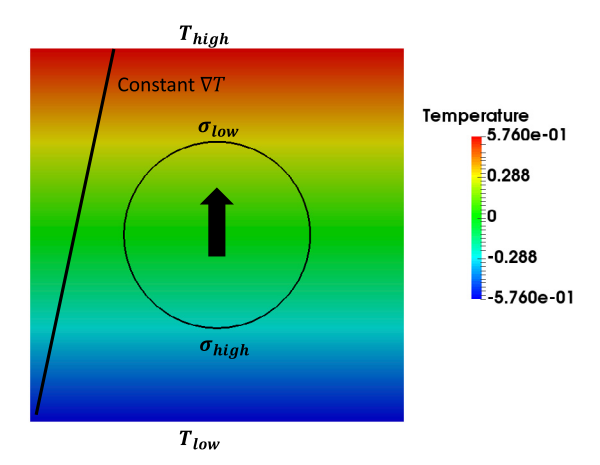


Fig. 3. Initial and boundary conditions for Marangoni driven flow problem.

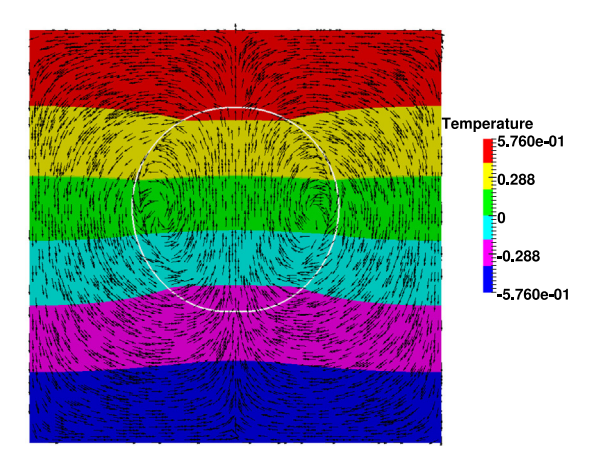


Fig. 4. Temperature and direction of the terminal velocity field.

Two recirculation regions are then formed inside the droplet. The dimensionless rise velocity for each mesh is plotted against dimensionless time in Fig. 5a. As seen from the inset in Fig. 5a, it is clear that the results converge as the mesh is refined.

In addition, Fig. 5b plots the dimensionless rise velocity against dimensionless time for both the present work and the results obtained from Ma and Bothe [52] when using the same structured quadrilateral mesh. The transient dimensionless rise velocity predicted from our model agree well with those obtained by Ma and Bothe.

4.2. Additive manufacturing benchmark test series

The National Institute of Standards and Technology (NIST) laboratory performed series of Additive Manufacturing Benchmark (AM-Bench) tests [53]; these included a series of highly controlled additive manufacturing benchmark tests resulting in experimental data that can be used to validate numerical models aimed at elucidating detailed physical phenomena associated with additive manufacturing [54]. For this manuscript, an AM-Bench experiment measuring process behavior for individual laser tracks on bare Inconel 625 (IN625) substrates will be used as a source of validation data for our thermal multiphase solver.

At NIST, an EOS M270 machine was used to produce single track scans on the bare IN625 substrate. A 1070-nm continuous wave laser with a beam diameter of 100 μ m is used to melt the bare plate; the beam diameter is defined as the width at which the Gaussian beam intensity is $1/e^2$ or approximately 13.5% of its nominal value. Low-velocity gas flow consisted of nitrogen and 0.5% oxygen. Three separate cases with different beam powers and scanning

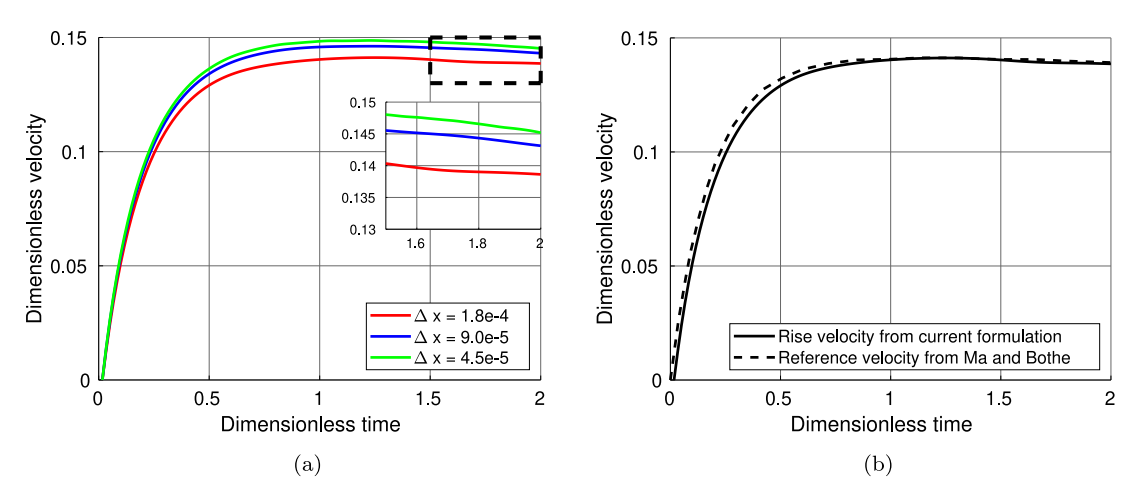


Fig. 5. (a) Time evolution for dimensionless rise velocity for 3 different element sizes and (b) comparison between results from the current implementation compared with those of Ma and Bothe [52] using 16 elements across the diameter of the droplet.

Table 1
Laser powers and scanning speeds for each case for the AM-Bench IN625 bare plate scan.

Case	Laser power (W)	Scan speed (mm/s)
A	150	400
В	195	800
C	195	1200

speeds were done for this experiment. The experimental parameters for each case are shown in Table 1. High-speed short-wave infrared (SWIR) cameras were used for in-situ measurements of melt pool lengths and solid cooling rates near the melt pool. These measurements in the melt pool lengths and solid cooling rates will be used as a comparison against our simulation. The solid cooling rate \hat{T}_{solid} is computed as

$$\dot{T}_{solid} = \frac{T_{solid} - 1273 \text{ K}}{\Delta t_{cool}} = \frac{(T_{solid} - 1273 \text{ K}) V_s}{\Delta d}$$

$$(55)$$

where T_{solid} is the solidus temperature and Δt_{cool} is the cooling time interval it takes to cool from T_{solid} to 1273 K. As seen in Eq. (55), Δt_{cool} can also be determined by dividing the distance Δd between the $T = T_{solid}$ and T = 1273 K isotherm by the scan speed V_s . Inconel 625 material properties are listed in Table 2. A 6 × 1 × 1 mm domain is discretized with an unstructured hexahedral mesh of 1.5 million elements and 1.6 million nodes with the finest element size being 10 μ m. A time step of $\Delta t = 1$ μ s is used.

The predicted free surface at steady state is shown in Fig. 6 for Case C. Fig. 6a shows the results when applying the turbulence model described in Section 2.7, whereas Fig. 6b shows the results without the turbulence model. The solidus and T = 1273 K isotherm, which are used to calculate \dot{T}_{solid} in Eq. (55), are colored in black and white, respectively. The melt pool is defined by the solidus isotherm. Fig. 7 shows the time history for both the melt pool length and cooling rate defined in Eq. (55) for case C. Fig. 7a shows that incorporating the turbulence results in a very steady melt pool; omitting this model results in similar results with a small fluctuation at the beginning of the simulation, and then reaching a steady state after a sufficient amount of time. This same behavior is observed in the computed cooling rates in Fig. 7b.

As seen from Fig. 6b, there is a larger free surface deformation when omitting the turbulence model. The addition of a turbulence model provides enhanced momentum and heat transport through the turbulent conductivity k_T and viscosity μ_T , respectively. Enhancing the heat transport reduces the thermal gradients near the keyhole wall, which mitigates the free surface forces causing deformation. In addition, Fig. 6 shows the predicted melt pool shapes with and without the turbulence model. Free surface forces are more dominant without the turbulence model, inducing a more localized flow and cooling behavior near the laser irradiation spot. When the turbulence model is added,

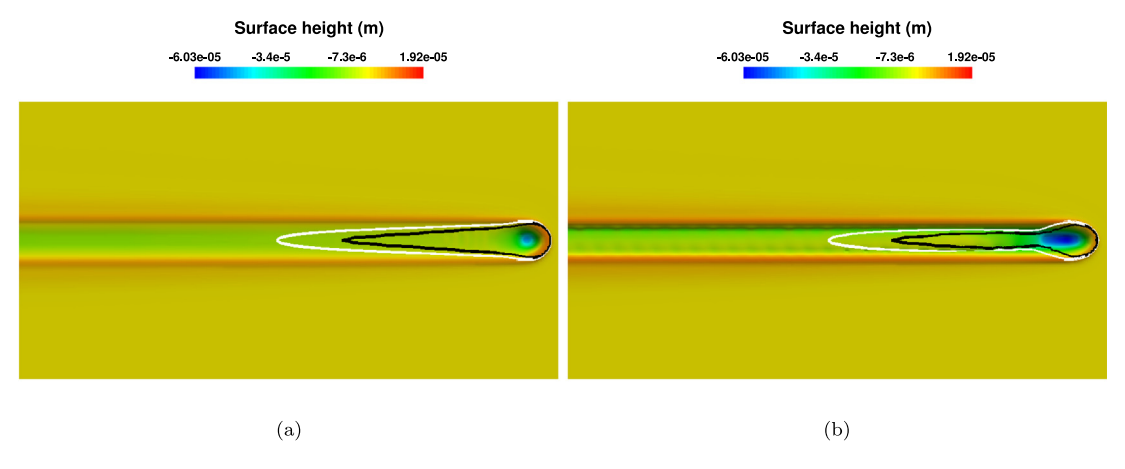


Fig. 6. Free surface evolution of AM Bench colored by the surface height for case C (a) with the turbulence model and (b) without the turbulence model. Solidus and 1273 K isotherms are colored in black and white, respectively.

Table 2
Thermo-physical properties of IN625.

Name	Property	Value
Solid density	$\rho_s\left(\frac{\mathrm{kg}}{\mathrm{m}^{-3}}\right)$	8440
Liquid density	$ ho_l\left(rac{\mathrm{kg}}{\mathrm{m}^{-3}} ight)$	7640
Gas density	$ \rho_g\left(\frac{\mathrm{kg}}{\mathrm{m}^{-3}}\right) $	0.894
Liquid viscosity	μ_l (Pa s)	6.0×10^{-3}
Gas viscosity	μ_g (Pa s)	3.6×10^{-5}
Solid specific heat	$c_{p,s}\left(\frac{J}{kgK}\right)$	550
Liquid specific heat	$c_{p,l}\left(\frac{\mathtt{J}}{\lg \mathtt{K}}\right)$	500
Gas specific heat	$c_{p,g}\left(\frac{\mathrm{J}}{\mathrm{kg}\;\mathrm{K}}\right)$	680
Solid thermal conductivity	$k_s\left(\frac{W}{mK}\right)$	10
Liquid thermal conductivity	$k_l\left(\frac{W}{mK}\right)$	23.2
Gas thermal conductivity	$k_g\left(\frac{W}{mK}\right)$	2.8×10^{-2}
Surface tension coefficient	$\sigma\left(\frac{N}{m}\right)$	1.8
Marangoni coefficient	$\frac{\partial \sigma}{\partial T} \left(\frac{N}{m K} \right)$	-3.7×10^{-4}
Latent heat of fusion	$L\left(rac{\mathrm{k}\mathrm{J}}{\mathrm{k}\mathrm{g}\;\mathrm{K}} ight)$	223
Latent heat of vaporization	$L_v\left(rac{\mathrm{kJ}}{\mathrm{kg}\;\mathrm{K}} ight)$	6465
Solidus temperature	T_S (K)	1563
Liquidus temperature	T_L (K)	1623
Evaporation temperature	T_{evap} (K)	3000
CTE	$\beta\left(\frac{1}{K}\right)$	8.0×10^{-6}
Emissivity	ϵ (1)	0.4
Stefan-Boltzmann constant	$\sigma_{SB}\left(rac{\mathrm{W}}{\mathrm{m}^2~K^4} ight)$	5.67×10^{-8}
Absorptivity	η (1)	0.445
Molar mass	$m_{mol} \left(\frac{g}{mol} \right)$	62.2

the enhanced thermal conductivity and viscosity act to spread both the thermal and flow field, resulting in a larger melt pool at the tail end.

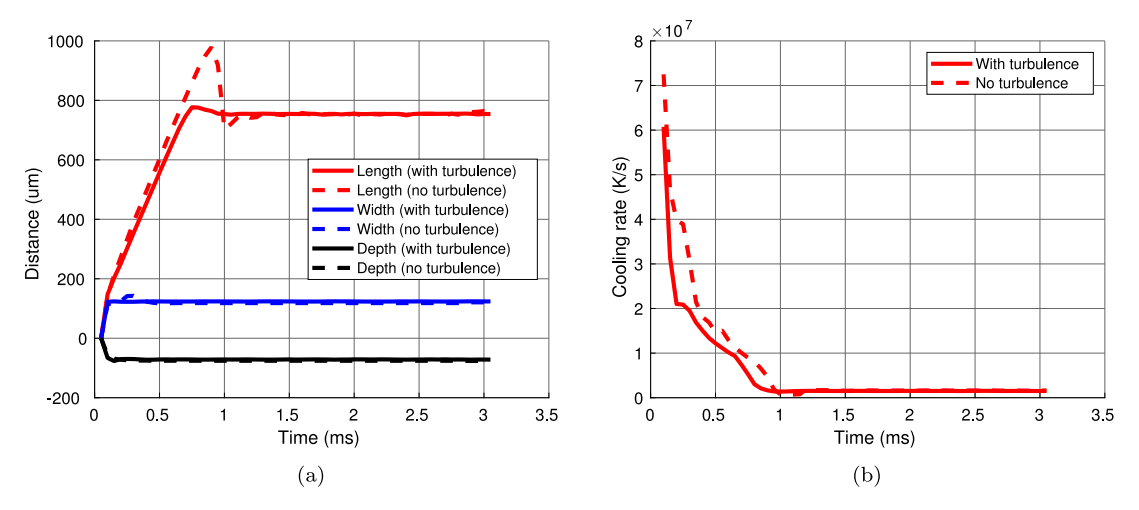


Fig. 7. (a) Melt pool dimensions over time and (b) cooling rate over time for AM Bench case C.

 Table 3

 Comparison of melt pool length between experiments and simulation.

	Length (µm) measured by experiment	Predicted length (μm) with turbulence	Predicted length (μm) without turbulence
Case	Value	Value (difference)	Value (difference)
A	659 ± 21	658 (0.1%)	614 (6.8%)
В	782 ± 21	795 (1.6%)	763 (2.4%)
C	754 ± 46	755 (0.1%)	753 (0.1%)

Table 4Comparison of solid cooling rate between experiments and simulation.

	Solid cooling rate (K/s) measured by experiment	Predicted solid cooling rate (K/s) with turbulence	Predicted solid cooling rate (K/s) without turbulence
Case	Value	Value (difference)	Value (difference)
A	$6.20 \pm 0.79 \times 10^5$	$7.11 \times 10^5 \ (14.6\%)$	$7.55 \times 10^5 \ (21.7\%)$
В	$9.35 \pm 1.43 \times 10^5$	$10.32 \times 10^5 (11.0\%)$	$11.54 \times 10^5 \ (23.4\%)$
C	$12.80 \pm 3.94 \times 10^5$	$15.20 \times 10^5 \ (18.7\%)$	$16.16 \times 10^5 \ (26.2\%)$

Table 3 compares the melt pool length predictions against experimentally observed lengths for all three cases. Predictions obtained with the turbulence model provide a good match with experimentally measured results; all cases predict a length that is within the range of uncertainty. Without the turbulence model the melt pool predictions yield a slightly larger error, with the length for Case A falling outside the range of uncertainty. Table 4 compares the computed cooling rate against the experimental measurements for all three cases. From this table it can be seen that predictions with the turbulence model yield a closer prediction to the experimental results than without the turbulence model; predictions with the turbulence model give differences with the experimental results below 19%, whereas predictions without the turbulence model give differences above 21%.

4.3. Single particle entrainment for DED processes

We now apply our proposed multiphase algorithm to model a single powder particle being deposited and melted onto the substrate. Fig. 8 shows the schematic and mesh used for this problem. As seen in Fig. 8a, an unstructured tetrahedral mesh is used to discretize the 0.6 mm \times 0.6 mm \times 0.65 mm domain, resulting in a total of 4.4×10^6 elements and 8.8×10^5 nodes with the finest element size being 7 μ m. A time step of $\Delta t = 0.1$ μ s is used. Fig. 8b shows the setup for this problem; a laser irradiates from the top surface, which is split into an inflow and outflow boundary. The inflow boundary condition has a prescribed cylindrical pipe channel inlet velocity magnitude u_p

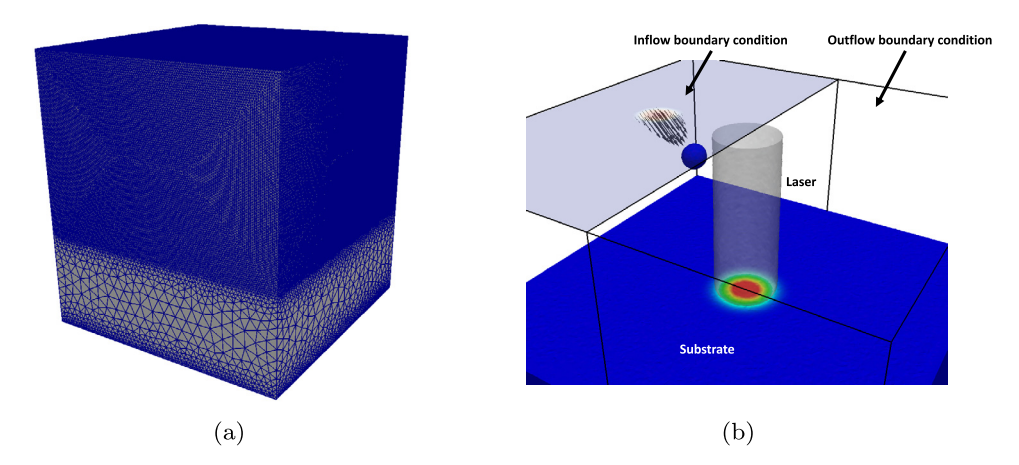


Fig. 8. Setup for single particle deposition with a stationary laser using (a) a tetrahedral mesh and (b) a mix of outflow and inflow boundary conditions.

defined as:

$$u_p(r_p) = \begin{cases} u_0 \left(1 - \left(\frac{r_p}{R_p} \right)^2 \right) & r_p \le R_p \\ 0 & r_p > R_p \end{cases}$$
 (56)

where r_p is the radial distance from some point to the center of the pipe, u_0 is the centerline pipe velocity and R_P is the pipe radius. This inlet condition is angled $\theta = 45^\circ$ towards the laser focal spot, resulting in $u_x = u_p \cos(\theta)$, $u_y = 0$ and $u_z = u_p \sin(\theta)$; there is a prescribed separation distance of 150 μ m between the inlet and the laser focal spot. The bottom surface is fixed at a temperature of 298 K with a no slip boundary condition on the velocity field. All other surfaces are outflow boundary conditions. The substrate and particle are both Ti-6Al-4V, with material properties shown in Table 5.

To enable motion of the powder particle, the Darcy term in Eq. (27) inhibiting velocity flow in solid phases is not applied above the height of the substrate. In addition, a high viscosity is assigned to the solid phases using Eq. (6). This treats solid powder particles above the substrate as a very viscous fluid that moves as a rigid body.

Fig. 9 shows a process of particle entrainment into the melt pool when using a centerline pipe inlet velocity of $u_0 = 45$ m/s and a powder particle radius of 20 μ m. The particle is initially outside of the laser irradiance zone in Fig. 9a. The particle eventually travels into the laser irradiance zone, as shown in Fig. 9b, and begins to heat up at the surface where the laser is being applied; a small section of the exposed surface reaches the evaporation temperature T_{evap} . A vapor jet forms at this surface, generating a recoil force that pushes the particle towards the melt pool, as seen in Fig. 9c. Fig. 9d shows that the particle melts and merges with the melt pool.

We now vary the centerline velocity u_0 to understand its effect on the entrainment process of a single particle. Centerline velocities of 45, 35 and 25 m/s are tested with a constant particle radius of 25 μ m. A similar set of simulations varying the particle radius are also performed; radii of 20, 25 and 30 μ m are simulated under a constant centerline velocity of $u_0 = 45$ m/s.

Fig. 10 shows the trajectory and velocity of the particle centroid when varying the centerline velocity u_0 . Fig. 10a shows that using the highest u_0 enables the powder particle to overcome the jet forming from evaporation at the laser focal spot, resulting in the particle penetrating closer to the focal spot of the laser. This allows a large surface of the particle to be heated to generate evaporative surface forces that drive the particle into the melt pool, as seen previously in Fig. 9. Decreasing u_0 lowers the particle's ability to penetrate this jet into the focal point of the laser, resulting in heating of a smaller portion of the particle surface, generating a more localized evaporation force at particle surface; this causes the particle to be pushed out of the laser irradiation zone and away from the melt pool, as seen for both $u_0 = 35$ and 25 m/s. Fig. 10b shows the velocity of the particle against time when varying u_0 . Decreasing u_0 results in a lower initial velocity of the particle. The velocity peaks in Fig. 10b show the time at which the evaporative forces on the particle surface begin to dominate the motion of the powder particle. The time until evaporative surfaces begin to dominate the particle motion increases with decreasing u_0 . Between $u_0 = 45$

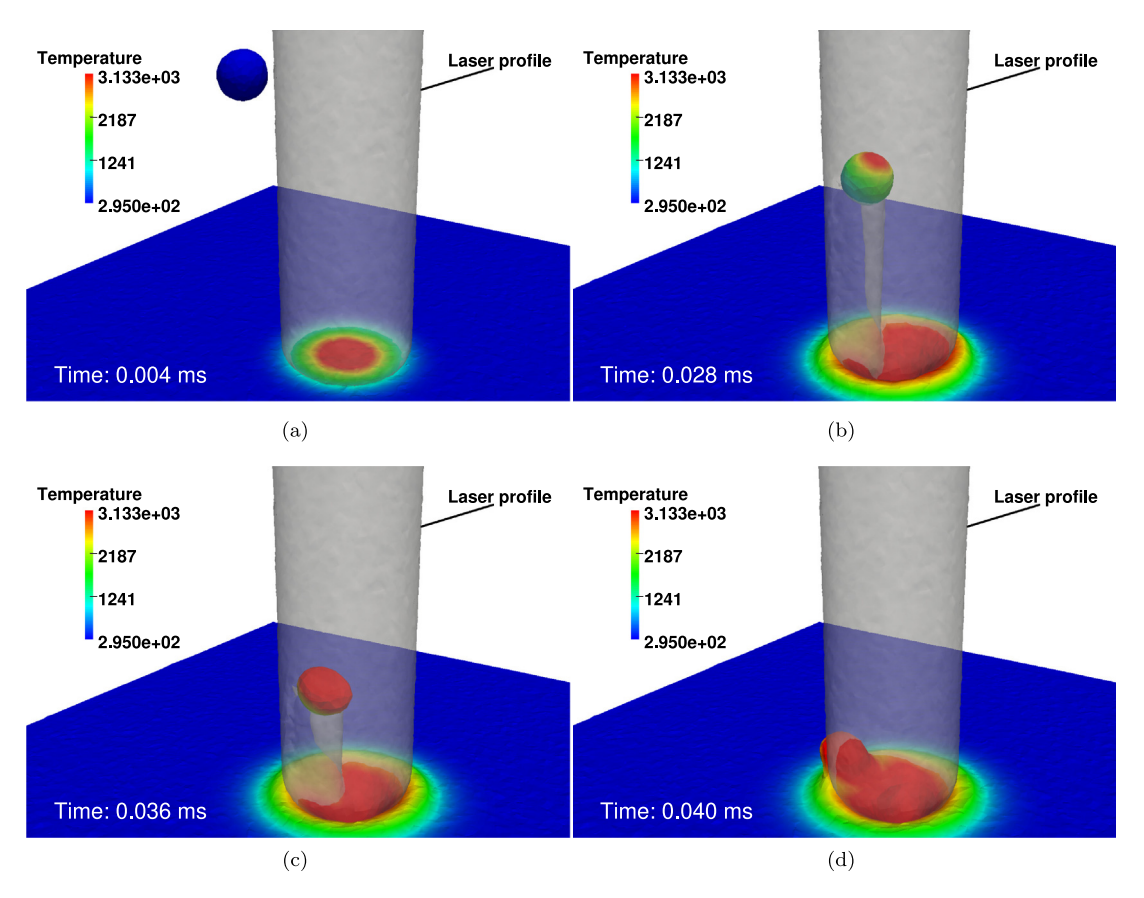


Fig. 9. DED process simulation showing single powder particle being delivered into laser focal spot at times (a) 0.004 ms (b) 0.028 ms (c) 0.036 ms and (d) 0.04 ms. An inlet centerline velocity of $v_0 = 45$ m/s and particle radius of 20 µm is used.

and $u_0 = 35$ m/s, we see that the peak velocity decreases with decreasing u_0 ; this is because a smaller surface area of the particle is irradiated to evaporation temperatures, thus decreasing the total evaporative force on the powder particle. However, this trend does not continue between $u_0 = 45$ and $u_0 = 35$ m/s; this is because the particle is merged into the melt pool, as seen in Fig. 10a, thus the particle does not travel far enough to generate a higher velocity.

Fig. 11 shows the trajectory and velocity of the particle centroid when varying the radius of the particle under a constant $u_0 = 45$ m/s. Fig. 11a shows that using a particle radius of 25 and 30 μ m results in the particle being ejected from the laser irradiance zone. The trajectories for both these particles show little difference. This stems from larger particles partially bonding with the melt pool and the solid substrate as the evaporative forces begin to displace the particle, as seen in Fig. 12. The remaining particle material cools through conduction with the substrate and solidifies near the melt pool. The velocity of each particle size is shown in Fig. 11b; the initial and peak velocities of these particles do not differ much either. This is because the surrounding vapor field induces particle motion rather than the forces generated from the velocity acting on the surface of the particle; thus using a constant u_0 for all cases results in a similar initial velocity for all powder particles. The peak velocities for each case in Fig. 11b are also similar. This is because the particles travel a short distance before they become either melted and merged into the molten melt pool (for a 20 μ m radius particle) or hit the substrate and cool through conduction; this restricts their acceleration.

4.4. Modeling a multi-particle DED process

We now model a DED process depositing multiple powder particles onto the substrate. Fig. 13 shows the mesh and boundary conditions used to model this process. As seen in Fig. 13a, an unstructured tetrahedral mesh is used

Table 5Thermo-physical properties of Ti-6Al-4V

Name	Property	Value
Solid density	$\rho_s\left(\frac{\mathrm{kg}}{\mathrm{m}^{-3}}\right)$	4000
Liquid density	$ \rho_l \left(\frac{\mathrm{kg}}{\mathrm{m}^{-3}} \right) $	4000
Gas density	$ \rho_g\left(\frac{\mathrm{kg}}{\mathrm{m}^{-3}}\right) $	0.894
Solid viscosity	μ_s (Pa s)	2
Liquid viscosity	μ_l (Pa s)	5×10^{-3}
Gas viscosity	μ_g (Pa s)	1.5×10^{-5}
Solid specific heat	$c_{p,s}\left(\frac{J}{kgK}\right)$	670
Liquid specific heat	$c_{p,l}\left(\frac{\mathtt{J}}{\lg \mathtt{K}}\right)$	730
Gas specific heat	$c_{p,g}\left(\frac{\mathrm{J}}{\mathrm{kg}\;\mathrm{K}}\right)$	680
Solid thermal conductivity	$k_s\left(\frac{W}{mK}\right)$	21
Liquid thermal conductivity	$k_l\left(\frac{W}{mK}\right)$	29
Gas thermal conductivity	$k_g\left(\frac{W}{mK}\right)$	2.8×10^{-2}
Surface tension coefficient	$\sigma\left(\frac{N}{m}\right)$	1.4
Marangoni coefficient	$\frac{\partial \sigma}{\partial T} \left(\frac{N}{m K} \right)$	$-2.6 \times 10^{-}$
Latent heat of fusion	$L\left(\frac{\mathrm{kJ}}{\mathrm{kg}\;\mathrm{K}}\right)$	369
Latent heat of vaporization	$L_v\left(\frac{\mathrm{kJ}}{\mathrm{kg}\;\mathrm{K}}\right)$	4700
Solidus temperature	T_S (K)	1878
Liquidus temperature	T_L (K)	1928
Evaporation temperature	T_{evap} (K)	3133
CTE	$\beta\left(\frac{1}{K}\right)$	8.0×10^{-6}
Emissivity	ϵ (1)	0.4
Stefan-Boltzmann constant	$\sigma_{SB}\left(rac{\mathrm{W}}{\mathrm{m}^2\ K^4} ight)$	$5.67 \times 10^{-}$
Molar mass	$m_{mol} \left(\frac{g}{\text{mol}} \right)$	44.6

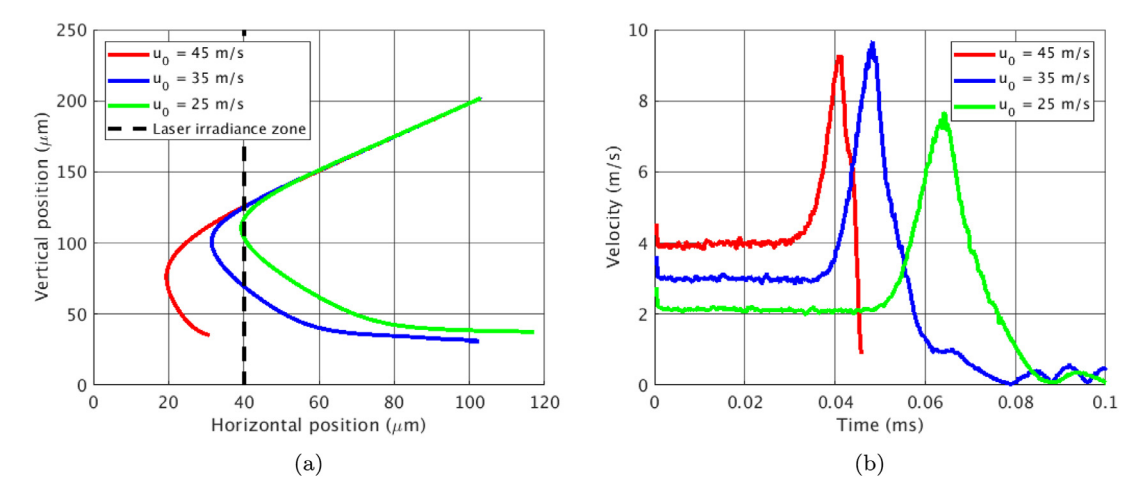


Fig. 10. (a) Spatial trajectory and (b) velocity of the particle centroid under varying centerline inlet velocities u_0 with a constant particle radius $20 \mu m$.

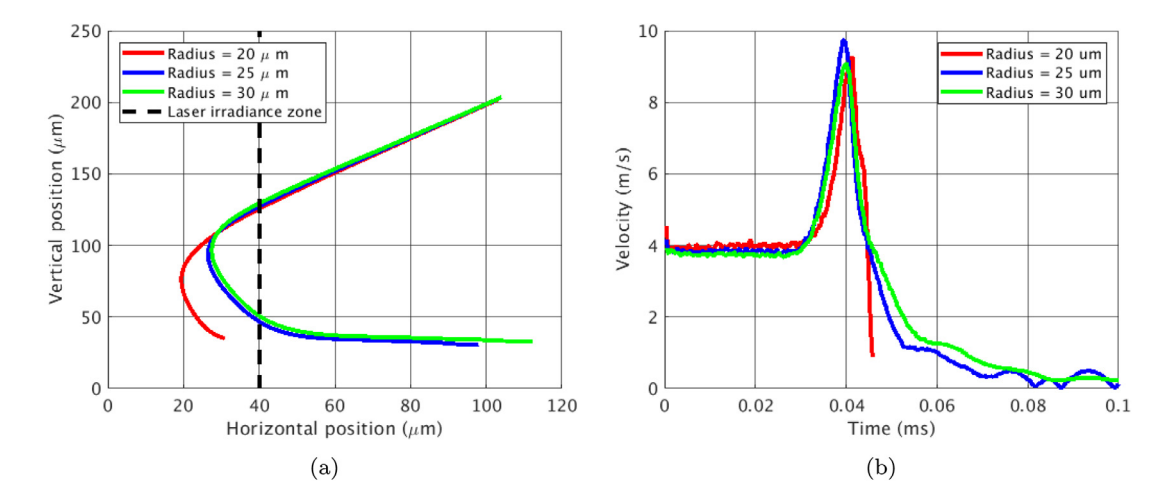


Fig. 11. (a) Spatial trajectory and (b) velocity of the particle centroid under varying particle radii with a constant centerline inlet velocity $u_0 = 45$ m/s.

to discretize the domain; the mesh contains 3,185,151 elements and 657,161 nodes, with the finest element size being 7 μ m. A time step of $\Delta t = 0.2~\mu$ s is used. Fig. 13b shows the setup for this model. Like the single particle entrainment case in Section 4.3, the top boundary is split into an inflow and outflow boundary, with a laser irradiating from the top surface. For this example, the laser moves in a straight line across the substrate at a scan speed of 300 mm/s. The laser has a radius of 40 μ m, a power of 250 W, and an absorptivity η of 0.3. The pipe channel inlet velocity in Eq (56) is used for the inflow boundary condition, and has a centerline velocity u_0 of 25 m/s and is angled at 45° behind the laser; this inflow condition linearly moves with the laser at a separation distance of 100 μ m.

To model powder deposition into the computational domain, we make a simplification and assume individual particles are injected one by one near the position of the moving inlet velocity; the surrounding vapor flow then carries the particle towards the laser focal spot. Powders are injected periodically into the domain every 40 μ s; the injection of individual particles is done by merging the most recently computed level set and volume fraction field with a spherical profile with a predetermined radius. For this example, all particles injected into the domain have a radius of 20 μ m. Over 0.5 ms, a total of 12 particles are injected and entrained into the melt pool. Both the particles being deposited and the substrate are Ti-6Al-4V; thermo-physical material properties for this material are listed in Table 5.

Fig. 14 shows a cross-section of the entrainment of a powder particle during the multi-particle DED simulation. Each snapshot visualizes the laser irradiating on the free surface of the Ti-6Al-4V material, the vapor plume generated by evaporation, and the free surface evolution contoured by the temperature field. The particle entrainment process shown here is similar to that shown in Section 4.3. Fig. 14a shows the particle being injected into the domain. In Fig. 14b, the particle becomes irradiated by the laser and heats up. The particle travels towards the center of the laser in Fig. 14c, and becomes further heated and reaches the evaporation temperature T_{evap} ; evaporation occurs, forming a jet on the surface of the particle to generate a recoil force that pushes the particle towards the melt pool, as seen in Fig. 14d. The particle then melts and merges with the melt pool.

This simulation also visualizes the laser shielding process from flowing particles interacting with the laser; prior experiments [16,55] showed that this had a large effect on the melt pool evolution. Fig. 14a shows the melt pool temperature distribution in the vicinity is at the evaporation temperature and has formed a keyhole. The powder particle absorbs the laser in Fig. 14b, shielding the laser absorption into the melt pool; this is reflected in the decrease temperature at the rear of the keyhole wall which is directly below the flowing particles. Fig. 14c shows that the particle has obstructed a large portion of laser traveling into the melt pool; this further reduces the temperature of the keyhole wall as now only a small portion at the front of the keyhole wall is at the evaporation temperature. Finally, in Fig. 14c the particle becomes entrained towards the back of the melt pool, enabling a larger portion of the keyhole front wall to be irradiated by the laser and heat back up to the evaporation temperature.

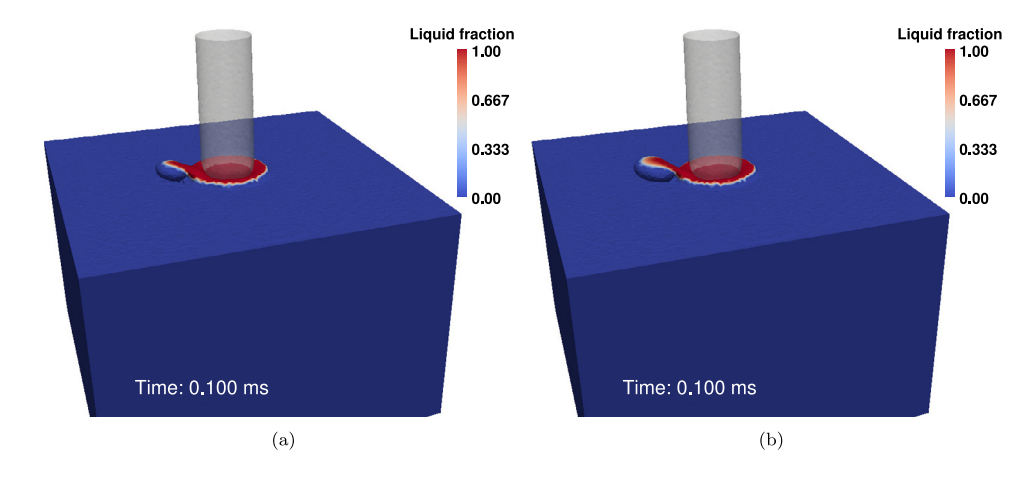


Fig. 12. Final frame of single particle simulation colored by liquid fraction f_L with $u_0 = 45$ m/s and a particle radius of (a) 25 μ m and (b) 30 μ m.

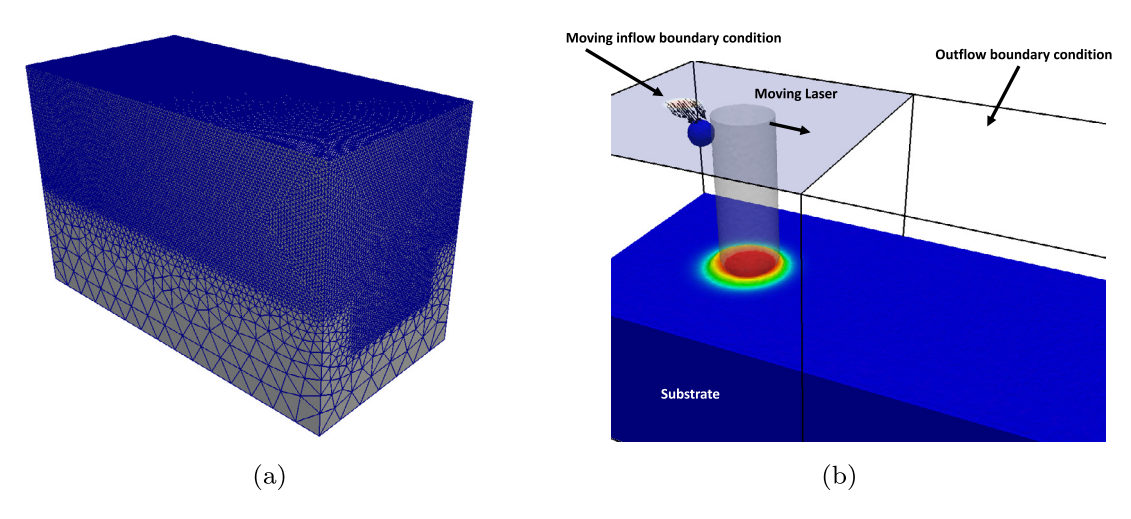


Fig. 13. Setup for multiple particle deposition with a moving laser using (a) a tetrahedral mesh and (b) a mix of outflow and inflow boundary conditions.

A separate simulation using the same material properties and boundary conditions of the multi-particle DED simulation is run without the deposition of powder particles; this effectively is a laser scanning on a bare plate of Ti-6Al-4V. This simulation is run to compare the effects of the aforementioned laser shielding process on the evolution of the melt pool geometry. Fig. 15 shows the cross sections of both simulation at t = 0.5 ms, visualizing both the free surface and melt pool evolution; the melt pool geometry is defined by the solidus temperature isotherm. Fig. 15a shows that inclusion of particle deposition results in a shallower and longer melt pool than the case with no particle deposition, as seen in Fig. 15b. Fig. 16 plots the melt pool dimensions of both simulations over time. It can be seen that the melt pool becomes longer, wider and shallower when particles are deposited. During the particle deposition process, the energy from the laser is delivered onto the top surface of the melt pool through its collision with heated powder particles. This generates large thermal gradients on the top free surface of the melt pool, inducing a backward and outward flow from the Marangoni force to enlarge the top surface area of the melt pool. When there is no particle deposition, the laser is absorbed directly into the substrate; enough energy is absorbed to form a keyhole within the melt pool, which then collects the incident laser flux at the bottom to create a deeper and shorter melt pool. This type of behavior has been observed experimentally [56], where an increase in mass flow rate of powder particles decreased the melt pool depth but increased the melt pool length.

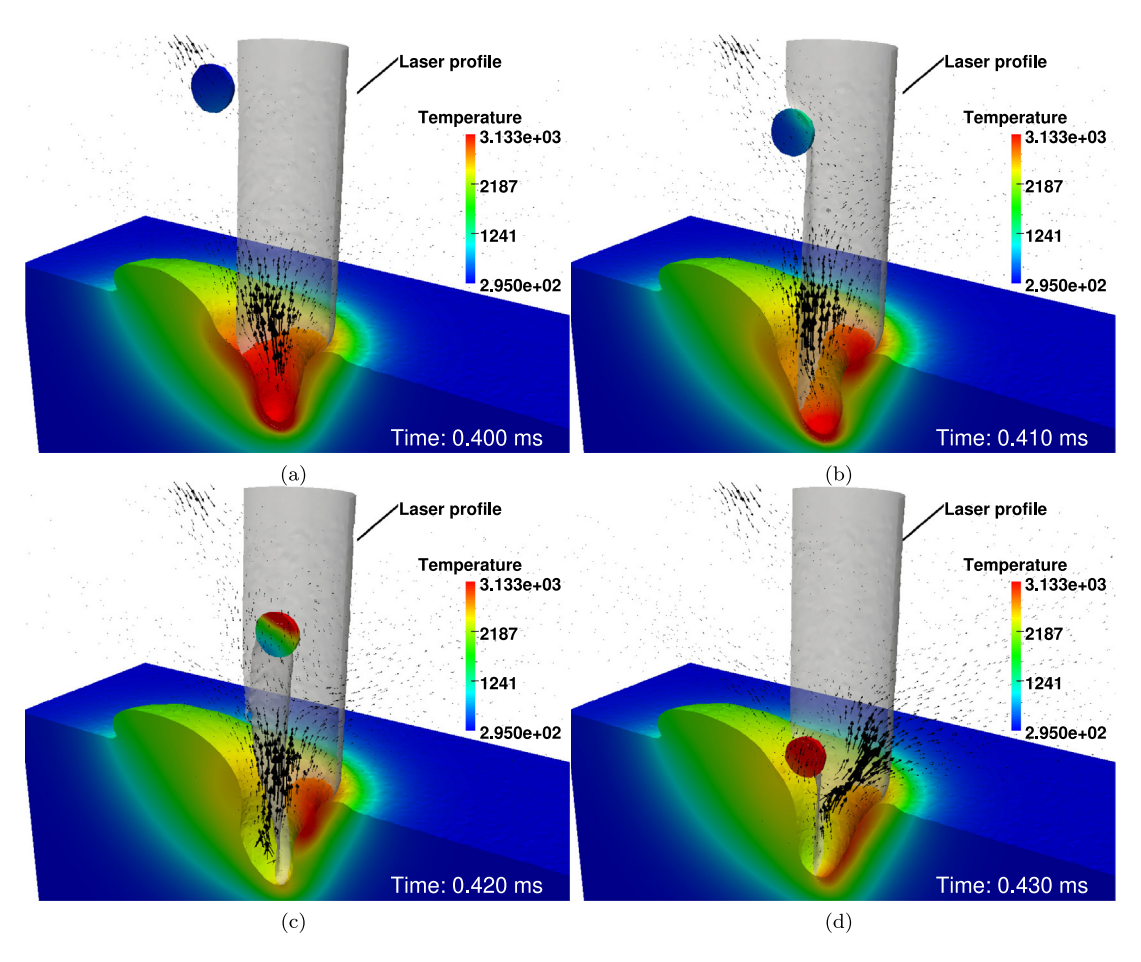


Fig. 14. Images of a DED process simulation depositing 1 out of 12 particle particles into the melt pool with a uni-directional laser scan at times (a) 0.40 ms (b) 0.41 ms (c) 0.42 ms and (d) 0.43 ms.

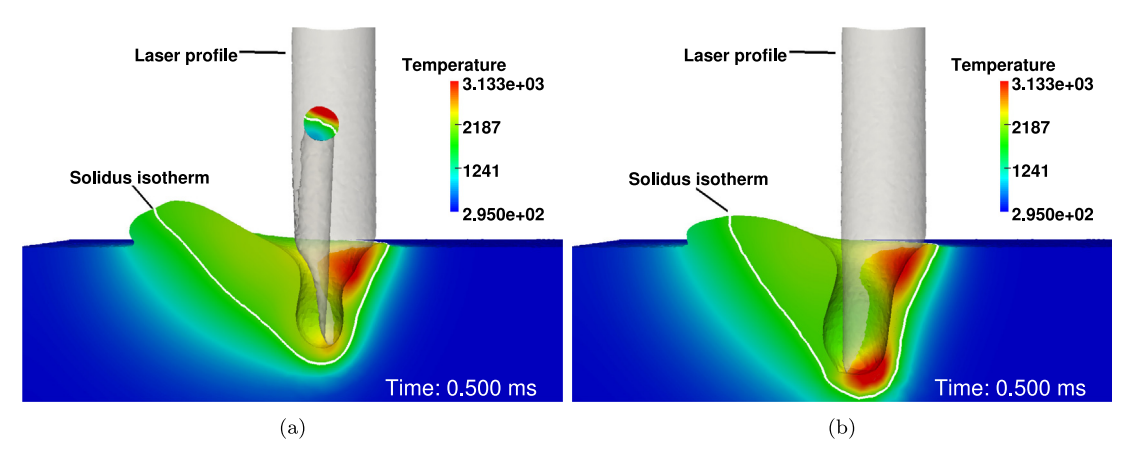


Fig. 15. Cross section of free surface and melt pool evolution of (a) DED process with particle deposition and (b) bare plate with no material deposition.

Lastly, we rerun the multi-particle DED example using a hexahedral mesh, and compare the predicted melt pool dimensions against the predictions obtained using the tetrahedral mesh. The simulation is run until a time of

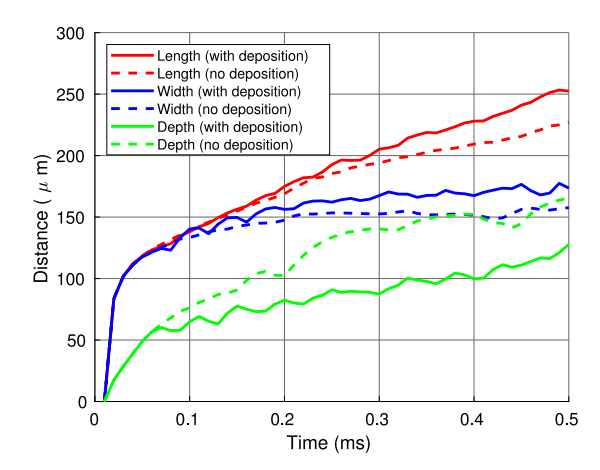


Fig. 16. Comparison of predicted melt pool dimensions over time for a DED process depositing 12 particles and a bare plate scan (no particle deposition).

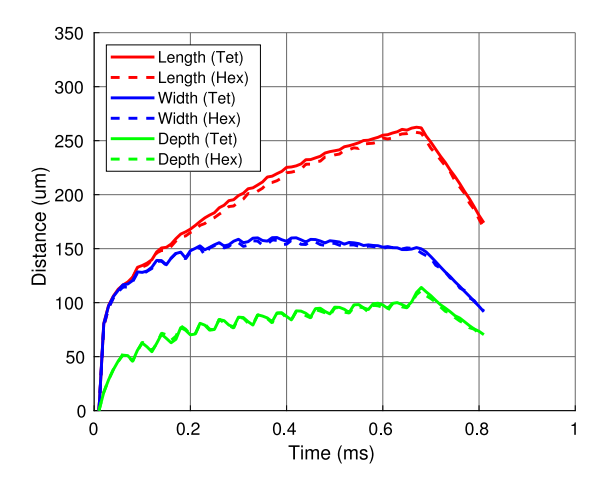


Fig. 17. Predicted melt pool dimensions over time for a DED process depositing 20 particles with a hexahedral and a tetrahedral mesh.

t=0.8 ms, resulting in a deposition of 20 particles. In addition, the laser power is decreased to 210 W to decrease the keyhole evolution. A tetrahedral mesh with 8.5×10^6 elements, 1.6×10^6 nodes and the finest element size of 5 μ m is compared with a structured hexahedral mesh with a uniform element size of 5 μ m, 1.2×10^6 elements and 1.5×10^5 nodes. Fig. 17 shows the predicted melt pool dimensions over time for both the tetrahedral and the hexahedral mesh. These results show that the proposed thermal multiphase model is applicable to both structured and unstructured meshes.

5. Conclusion

We have presented a novel multiphase thermo-fluid model in a control volume finite element formulation. This enables us to model the transient free surface, fluid flow, thermal, phase and laser-material interaction evolution throughout the DED processes.

This multiphysics and multiphase formulation is applied to a benchmark problem (Section 4.1) and bare plate scan (Section 4.2) to assess its accuracy; results from our proposed formulation provide a good agreement with predicted benchmark solutions from literature and experimentally measured quantities, respectively. We then model simple DED processes. Section 4.3 shows the deposition and eventual melt pool entrainment of a single powder. A parametric study shows that a larger velocity carrying the deposited powder will assist in the penetration of the powder towards the focal spot of the laser; the resulting laser absorption will induce evaporation across a larger

surface of the powder to drive powder motion either into or outside of the melt pool. Section 4.4 demonstrates our model on a DED process within a moving laser depositing multiple powder particles. Results from these simulations show that the addition of powder material can have a large effect on the melt pool dimensions; it was found that in-flight particles shielding the melt pool from laser absorption had a large effect on mitigating the keyhole evolution within the melt pool.

There are areas of our framework that can be improved. For example, Section 4.3 shows that the current method of delivering particles towards the melt pool uses the ambient vapor flow to carry the powder towards the laser focal spot, which may not be representative of the real DED process. A more accurate method may consider the force imparted to the powder surface from the fluid–structure interaction with the ambient vapor. In addition, our current model for laser-material interaction provides a robust approach for understanding effects of laser-shielding from in-flight powders as well as full absorption into the melt pool to generate a keyhole; this model can be improved, however, to incorporate reflection from material free surfaces. This may provide a more accurate energy distribution imparted onto the substrate in keyhole regimes, where a larger keyhole collects more energy. Lastly, Section 4.4 demonstrates that unstructured meshes do not degrade accuracy, indicating an opportunity for the proposed formulation to be combined with adaptive mesh refinement technology to reduce computational cost. This is especially useful for modeling the fusion of multiple layers in a DED process. Systematic studies on a few layers may provide an analysis that is relevant to production-scale builds to inform the selection of input processing parameters of AM.

Declaration of competing interest

The authors declare that they have no known competing financial interests or personal relationships that could have appeared to influence the work reported in this paper.

Acknowledgments

This work was supported in part by National Science Foundation (NSF), USA Cyber–Physical Systems (CPS) under Grant No. CPS/CMMI-1646592 and by the Center for Hierarchical Materials Design (CHiMaD), USA under Grant No. 70NANB19H005. Stephen Lin is supported by the National Science Foundation Graduate Research Fellowship under Grant No. DGE-1324585.

Appendix

Consider fluid in the vicinity of a liquid–gas interface moving with velocity u^* . Then, in a frame of reference moving with the interface, the fluid satisfies a steady mass conservation equation of the form

$$\nabla \cdot \rho(\mathbf{u} - \mathbf{u}^*) = 0 \tag{A.1}$$

which after some rearrangement can be written

$$\nabla \cdot \boldsymbol{u} = -\frac{\boldsymbol{u} - \boldsymbol{u}^*}{\rho} \cdot \nabla \rho \tag{A.2}$$

Ignoring the solid phase, by Eq. (6) the density can be written as

$$\rho = H_{\varepsilon}(\phi)\rho_l + (1 - H_{\varepsilon}(\phi))\rho_g = \rho_g - H_{\varepsilon}(\phi)[\rho] \tag{A.3}$$

where $[\rho] = \rho_g - \rho_l$ is the change in density across the interface. The density gradient, then, is given by $\nabla \rho = -[\rho] H'_{\varepsilon}(\phi) \mathbf{n}$ where we have used $\nabla \phi = \mathbf{n}$. The evaporative mass flux m_{evap} is given by $\rho (\mathbf{u} - \mathbf{u}^*) \cdot \mathbf{n}$, so Eq. (A.2) can finally be rewritten as

$$\nabla \cdot \boldsymbol{u} = \frac{m_{evap}}{\rho^2} [\rho] H_{\varepsilon}'(\phi) \tag{A.4}$$

It is straightforward to show that this is equivalent to Eq. (26), which is written and implemented most conveniently in terms of $\nabla (1/\rho)$.

References

- [1] S.A. Khairallah, A. Anderson, Mesoscopic simulation model of selective laser melting of stainless steel powder, J. Mater Process. Technol. 214 (11) (2014) 2627–2636.
- [2] S.A. Khairallah, A.T. Anderson, A. Rubenchik, W.E. King, Laser powder-bed fusion additive manufacturing: Physics of complex melt flow and formation mechanisms of pores, spatter, and denudation zones, Acta Mater. 108 (2016) 36–45.
- [3] C. Körner, E. Attar, P. Heinl, Mesoscopic simulation of selective beam melting processes, J. Mater Process. Technol. 211 (6) (2011) 978–987.
- [4] C. Körner, A. Bauereiß, E. Attar, Fundamental consolidation mechanisms during selective beam melting of powders, Modelling Simulation Mater. Sci. Eng. 21 (8) (2013) 085011.
- [5] E. Attar, C. Körner, Lattice boltzmann model for thermal free surface flows with liquid-solid phase transition, Int. J. Heat Fluid Flow 32 (1) (2011) 156–163.
- [6] A. Klassen, A. Bauereiß, C. Körner, Modelling of electron beam absorption in complex geometries, J. Phys. D: Appl. Phys. 47 (6) (2014) 065307.
- [7] W. Yan, W. Ge, Y. Qian, S. Lin, B. Zhou, W.K. Liu, F. Lin, G.J. Wagner, Multi-physics modeling of single/multiple-track defect mechanisms in electron beam selective melting, Acta Mater. 134 (2017) 324–333.
- [8] W. Yan, Y. Qian, W. Ge, S. Lin, W.K. Liu, F. Lin, G.J. Wagner, Meso-scale modeling of multiple-layer fabrication process in selective electron beam melting: Inter-layer/track voids formation, Mater. Des. 141 (2018) 210–219.
- [9] C. Panwisawas, C. Qiu, M.J. Anderson, Y. Sovani, R.P. Turner, M.M. Attallah, J.W. Brooks, H.C. Basoalto, Mesoscale modelling of selective laser melting: Thermal fluid dynamics and microstructural evolution, Comput. Mater. Sci. 126 (2017) 479–490.
- [10] H.G. Weller, G. Tabor, H. Jasak, C. Fureby, A tensorial approach to computational continuum mechanics using object-oriented techniques, Comput. Phys. 12 (6) (1998) 620–631.
- [11] F.-J. Gürtler, M. Karg, K.-H. Leitz, M. Schmidt, Simulation of laser beam melting of steel powders using the three-dimensional volume of fluid method, Physics Procedia 41 (2013) 881–886.
- [12] M. Megahed, H.-W. Mindt, B. Shula, A. Peralta, J. Neumann, Powder bed models-numerical assessment of as-built quality, in: 57th AIAA/ASCE/AHS/ASC Structures, Structural Dynamics, and Materials Conference, 2016, p. 1657.
- [13] H.-W. Mindt, O. Desmaison, M. Megahed, A. Peralta, J. Neumann, Modeling of powder bed manufacturing defects, J. Mater. Eng. Perform. 27 (1) (2018) 32–43.
- [14] J.R.I. Medina, Development and Application of a CFD Model of Laser Metal Deposition (Ph.D. thesis), The University of Manchester (United Kingdom), 2013.
- [15] S.M.H. Hojjatzadeh, N.D. Parab, W. Yan, Q. Guo, L. Xiong, C. Zhao, M. Qu, L.I. Escano, X. Xiao, K. Fezzaa, W. Everhart, T. Sun, C. Lianyi, Pore elimination mechanisms during 3D printing of metals, Nature Commun. 10 (1) (2019) 3088.
- [16] S.J. Wolff, H. Wu, N. Parab, C. Zhao, K.F. Ehmann, T. Sun, J. Cao, In-situ high-speed x-ray imaging of piezo-driven directed energy deposition additive manufacturing, Sci. Rep. 9 (1) (2019) 962.
- [17] S. Ly, A.M. Rubenchik, S.A. Khairallah, G. Guss, M.J. Matthews, Metal vapor micro-jet controls material redistribution in laser powder bed fusion additive manufacturing, Sci. Rep. 7 (1) (2017) 4085.
- [18] S. Lin, J. Yan, D. Kats, G.J. Wagner, A volume-conserving balanced-force level set method on unstructured meshes using a control volume finite element formulation, J. Comput. Phys. 380 (2019) 119–142.
- [19] S. Osher, J.A. Sethian, Fronts propagating with curvature-dependent speed: algorithms based on hamilton-jacobi formulations, J. Comput. Phys. 79 (1) (1988) 12–49.
- [20] S. Osher, R. Fedkiw, Level Set Methods and Dynamic Implicit Surfaces, Springer-Verlag, New York, NY, 2002.
- [21] M. Sussman, P. Smereka, S. Osher, A level set approach for computing solutions to incompressible two-phase flow, J. Comput. Phys. 114 (1) (1994) 146–159.
- [22] E. Olsson, G. Kreiss, A conservative level set method for two phase flow, J. Comput. Phys. 210 (1) (2005) 225-246.
- [23] E. Olsson, G. Kreiss, S. Zahedi, A conservative level set method for two phase flow ii, J. Comput. Phys. 225 (1) (2007) 785-807.
- [24] B. Baliga, S. Patankar, A control volume finite-element method for two-dimensional fluid flow and heat transfer, Numer. Heat Transfer 6 (3) (1983) 245–261.
- [25] G. Schneider, M. Zedan, Control-volume-based finite element formulation of the heat conduction equation, Spacecr. Therm. Control Des. Oper. Prog. Astronaut. Aeronaut. 86 (1983) 305–327.
- [26] O. Desjardins, V. Moureau, H. Pitsch, An accurate conservative level set/ghost fluid method for simulating turbulent atomization, J. Comput. Phys. 227 (18) (2008) 8395–8416.
- [27] J. Brackbill, D.B. Kothe, C. Zemach, A continuum method for modeling surface tension, J. Comput. Phys. 100 (2) (1992) 335–354.
- [28] C.J. Knight, Theoretical modeling of rapid surface vaporization with back pressure, AIAA J. 17 (5) (1979) 519–523.
- [29] S.I. Anisimov, V.A. Khokhlov, Instabilities in Laser-Matter Interaction, CRC press, 1995.
- [30] G. Spencer, M. Murty, General ray-tracing procedure, JOSA 52 (6) (1962) 672-678.
- [31] J. Boussinesq, Théorie Analytique de la Chaleur Mise en Harmonic Avec la Thermodynamique et Avec la Théorie Mécanique de la Lumière: Tome I-[II]..., Vol. 2, Gauthier-Villars, 1903.
- [32] M. Courtois, M. Carin, P. Le Masson, S. Gaied, M. Balabane, A new approach to compute multi-reflections of laser beam in a keyhole for heat transfer and fluid flow modelling in laser welding, J. Phys. D: Appl. Phys. 46 (50) (2013) 505305.
- [33] M. Courtois, M. Carin, P. Le Masson, S. Gaied, M. Balabane, A complete heat and fluid flow modeling of keyhole formation and collapse during spot laser welding, in: International Congress on Applications of Lasers & Electro-Optics, Vol. 2013, LIA, 2013, pp. 77–84.

- [34] M. Courtois, M. Carin, P. Le Masson, S. Gaied, M. Balabane, A complete model of keyhole and melt pool dynamics to analyze instabilities and collapse during laser welding, 2014.
- [35] A. Esmaeeli, G. Tryggvason, Computations of film boiling. part i: numerical method, Int. J. Heat Mass Transfer 47 (25) (2004) 5451–5461.
- [36] V.R. Voller, M. Cross, N. Markatos, An enthalpy method for convection/diffusion phase change, Internat. J. Numer. Methods Engrg. 24 (1) (1987) 271–284.
- [37] F. Rösler, D. Brüggemann, Shell-and-tube type latent heat thermal energy storage: numerical analysis and comparison with experiments, Heat Mass Transfer 47 (8) (2011) 1027.
- [38] R. Rai, G. Roy, T. DebRoy, A computationally efficient model of convective heat transfer and solidification characteristics during keyhole mode laser welding, J. Appl. Phys. 101 (5) (2007) 054909.
- [39] D.C. Wilcox, et al., Turbulence Modeling for CFD, Vol. 2, DCW industries La Canada, CA, 1998.
- [40] T.J. Hughes, G. Engel, L. Mazzei, M.G. Larson, The continuous galerkin method is locally conservative, J. Comput. Phys. 163 (2) (2000) 467–488.
- [41] T.J. Hughes, G.N. Wells, Conservation properties for the galerkin and stabilised forms of the advection–diffusion and incompressible navier–stokes equations, Comput. Methods Appl. Mech. Engrg. 194 (9–11) (2005) 1141–1159.
- [42] S. Domino, "Sierra Low Mach Module: Nalu Theory Manual 1.0", SAND2015-3107W, Sandia National Laboratories Unclassified Unlimited Release(UUR), 2015, https://github.com/spdomin/NaluDoc.
- [43] V.R. Voller, Basic Control Volume Finite Element Methods for Fluids and Solids, Vol. 1, World Scientific, 2009.
- [44] A.J. Chorin, Numerical solution of the navier-stokes equations, Math. Comput. 22 (104) (1968) 745-762.
- [45] A.J. Chorin, On the convergence of discrete approximations to the navier-stokes equations, Math. Comput. 23 (106) (1969) 341-353.
- [46] A.S. Almgren, J.B. Bell, P. Colella, L.H. Howell, M.L. Welcome, A conservative adaptive projection method for the variable density incompressible navier–stokes equations, J. Comput. Phys. 142 (1) (1998) 1–46.
- [47] C. Rhie, W. Chow, Numerical study of the turbulent flow past an airfoil with trailing edge separation, AIAA J. 21 (11) (1983) 1525–1532.
- [48] F.N. Felten, T.S. Lund, Kinetic energy conservation issues associated with the collocated mesh scheme for incompressible flow, J. Comput. Phys. 215 (2) (2006) 465–484.
- [49] V. Voller, C. Swaminathan, Eral source-based method for solidification phase change, Numer. Heat Transfer B 19 (2) (1991) 175-189.
- [50] M. Heroux, R. Bartlett, V.H.R. Hoekstra, J. Hu, T. Kolda, R. Lehoucq, K. Long, R. Pawlowski, E. Phipps, A. Salinger, H. Thornquist, R. Tuminaro, J. Willenbring, A. Williams, An Overview of Trilinos, Technical Report SAND2003-2927, Sandia National Laboratories, 2003.
- [51] P. Lin, M. Bettencourt, S. Domino, T. Fisher, M. Hoemmen, J. Hu, E. Phipps, A. Prokopenko, S. Rajamanickam, C. Siefert, et al., Towards extreme-scale simulations with next-generation trilinos: a low mach fluid application case study, in: Parallel & Distributed Processing Symposium Workshops (IPDPSW), 2014 IEEE International, IEEE, 2014, pp. 1485–1494.
- [52] C. Ma, D. Bothe, Direct numerical simulation of thermocapillary flow based on the volume of fluid method, Int. J. Multiph. Flow. 37 (9) (2011) 1045–1058.
- [53] L.E. Levine, B. Lane, Additive manufacturing benchmark test series (am-bench), 2018.
- [54] Z. Gan, Y. Lian, S.E. Lin, K.K. Jones, W.K. Liu, G.J. Wagner, Benchmark study of thermal behavior, surface topography, and dendritic microstructure in selective laser melting of inconel 625, Integr. Mater. Manuf. Innov. (2019) 1–16.
- [55] J. Liu, L. Li, Effects of powder concentration distribution on fabrication of thin-wall parts in coaxial laser cladding, Opt. Laser Technol. 37 (4) (2005) 287–292.
- [56] K. Shah, A.J. Pinkerton, A. Salman, L. Li, Effects of melt pool variables and process parameters in laser direct metal deposition of aerospace alloys, Mater. Manuf. Process. 25 (12) (2010) 1372–1380.